Stochastic Pacing Inhibits Spatially Discordant Cardiac Alternans

Dan Wilson[1,*] and Bard Ermentrout[1]
[1]Department of Mathematics, University of Pittsburgh, Pittsburgh, Pennsylvania

ABSTRACT   Depressed heart rate variability is a well-established risk factor for sudden cardiac death in survivors of acute myocardial infarction and for those with congestive heart failure. Although measurements of heart rate variability provide a valuable prognostic tool, it is unclear whether reduced heart rate variability itself is proarrhythmic or if it simply correlates with the severity of autonomic nervous system dysfunction. In this work, we investigate a possible mechanism by which heart rate variability could protect against cardiac arrhythmia. Specifically, in numerical simulations, we observe an inverse relationship between the variance of stochastic pacing and the occurrence of spatially discordant alternans, an arrhythmia that is widely believed to facilitate the development of cardiac fibrillation. By analyzing the effects of conduction velocity restitution, cellular dynamics, electrotonic coupling, and stochastic pacing on the nodal dynamics of spatially discordant alternans, we provide intuition for this observed behavior and propose control strategies to inhibit discordant alternans.

INTRODUCTION

Heart rate variability (HRV) is a well-known prognostic indicator of a cardiac patient's susceptibility to sudden cardiac death, with lower HRV being positively correlated with higher mortality rates (1–6). Several statistics to describe HRV have been developed to quantify a patient's risk of sudden cardiac death. Such indicators include relatively straightforward time-domain measurements of the standard deviation of the cycle length (also referred to as the RR variability) (4) and spectral analysis of RR data (7), as well as more elaborate nonlinear indicators that use Lyapunov exponents (8), fractal scalings (9), and Poincaré maps (10). Beta blockers, a pharmacological intervention for those susceptible to ventricular fibrillation, are often used to reduce one's overall heart rate (HR) and have also been documented to increase HRV (11–13). Ivabradine, a newer medication for the treatment of heart failure, has also been shown to increase HRV (14,15). In some studies, a significant decrease in HRV immediately before the development of ventricular fibrillation has been reported (16–18), although in other studies this behavior was not observed (19–21).

Although depressed HRV has been shown to be predictive of a patient's risk of mortality due to sudden cardiac death, it is unknown whether loss of HRV is proarrhythmic, or

whether it is merely a symptom of autonomic nervous system dysfunction. For instance, the relationship between elevated resting HR and both all-cause and cardiovascular mortality is also well-established (22). Sudden cardiac death has been associated with high HRs (23), and in some studies, measurements of HR and HRV were found to be equally useful in their prognostic capabilities (24). Further complicating matters, it has been observed that HRV is inversely correlated with HR itself (25,26), making it difficult to disentangle their individual relationships with a patient's susceptibility to cardiac arrhythmia. Indeed, it has been observed that subpopulations of patients who display a significant decrease in HRV before the onset of arrhythmia also show a significant increase in HR in the same time frame (27). Subsequent studies have suggested that measures that take both HR and HRV into account may be useful for indicating that a ventricular fibrillation episode may be imminent (28).

In this work, we investigate a potential mechanistic link between depressed HRV and the propensity for the development of discordant alternans (DAs) in the heart, which is widely believed to be proarrhythmic via the development of a spatial dispersion of refractoriness in the cardiac tissue (29–35). Cardiac alternans is defined as the beat-to-beat alternation of electrochemical dynamics, which usually manifests in alternating long and short action-potential durations (APDs). Much work has been devoted to understanding the genesis of alternans at a cellular level, which is

CrossMark

usually attributed to either steep APD restitution (35,36), instability of the intracellular calcium dynamics (37,38), or a combination of both factors (39). In tissue, alternans can either be spatially concordant or discordant, with the former displaying APDs that are in phase throughout the tissue and the latter characterized by areas with long-short-long APD patterns neighboring areas with short-long-short APD patterns (see, e.g., Fig. 1 A). Steep conduction velocity (CV) restitution is generally implicated in the formation of discordant alternans (34,35,40,41), but other factors, such as premature or ectopic beats (35,42), as well as tissue heterogeneity (43), can play a role.

In laboratory conditions, the formation of cardiac alternans is generally investigated in vitro with a constant rate of pacing, or basic cycle length (BCL) (37,44–48), with changes to the BCL occurring only after steady-state dynamics have been reached. Such studies are imperative for understanding the deterministic mechanisms that underlie the formation of cardiac alternans. However, in normal human hearts, significant variability in the pacing rate is known to exist. For instance, in clinical studies, the standard deviation of successive differences between heart beats has been reported to be between 10 and 50 ms (12,49–52), as much as 5–7% of a healthy individual's nominal resting HR. Despite this fact, little emphasis has been given to un-

derstanding how alternans develops and is maintained for nonconstant pacing rates.

In healthy conditions, HRV can be affected on both slow and fast timescales due to factors such as circadian oscillations (53), environmental temperature fluctuations (54), respiration (55), and the effects of vagal activity (56). Each of these effects contribute to an overall power spectrum of HRV in the Fourier domain (57). In this work, we investigate a simpler situation where the cycle length is drawn from a Gaussian distribution. Other numerical (58) and experimental (59) studies have observed that in single cardiomyocytes, even small amounts of variance in the pacing rate can contribute to the formation of cardiac alternans, with the resulting interpretation that HRV might be proarrhythmic. Based on the results to follow, we come to a different conclusion: on one- (1-D) and two-dimensional (2-D) domains with single-site pacing in simulations of healthy, homogeneous, and isotropic ventricular tissue, as the variance in the pacing rate increases, the propensity for the tissue to exhibit discordant alternans decreases. Related results were obtained in 2-D simulations in a model where discordant alternans arises due to spatial gradients in the conductance of potassium channels (60). This behavior is reliably observed in models where alternans is driven by either steep APD restitution or instability in the
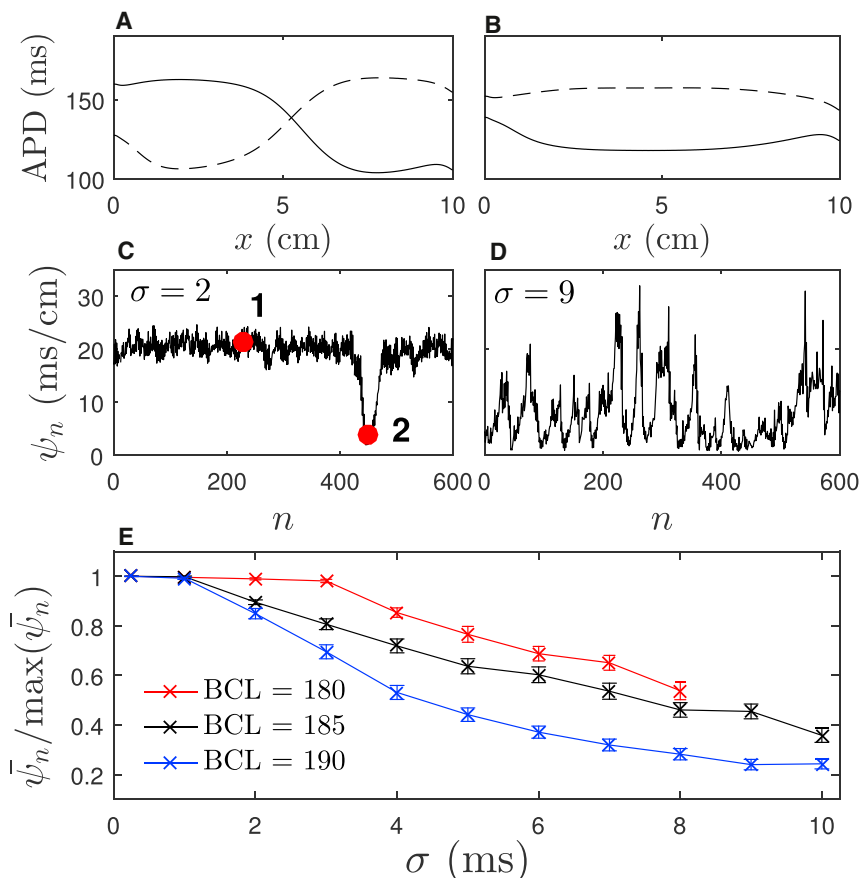

FIGURE 1 (A and B) APDs on the nth (solid line) and $n + 1$th (dashed line) beat during discordant and concordant alternans, respectively. Data are taken from simulations of Eq. 2 with $\sigma = 2$ ms and BCL = 185 ms. (C) Evolution of ψ_n, the maximal local dispersion of APDs, a function of the beat number, with points 1 and 2 corresponding to (A) and (B), respectively. (D) Results for the same system when $\sigma = 9$ ms. (E) Mean, $\overline{\psi}_n$ (crosses), and SE (bars) normalized by the maximal value of $\overline{\psi}_n$ as a function of σ for each BCL. To see this figure in color, go online.

intracellular calcium dynamics. These results suggest that sufficient HRV could protect against more serious cardiac arrhythmias such as ventricular fibrillation. In the simulations and analysis presented here, the transition from concordant to discordant alternans in homogeneous tissue occurs due to the interplay between APD and CV restitution. With theoretical analysis on the effect of stochastic pacing on both cellular alternans and nodal dynamics during discordant alternans, we provide intuition for the observation that stochastic pacing inhibits discordant alternans and suggest control strategies to discourage its formation.

METHODS

Numerical simulation of single cardiomyocytes

For single-cell numerical simulations, we use the Shiferaw-Fox model (61), which contains a detailed description of both cellular voltage dynamics and intracellular calcium cycling.

$$
\begin{aligned}
C_m \frac{dV}{dt} &= -(I_{\text{ion}}(V, m) + I_{\text{ext}}(t)), \\
\frac{dm}{dt} &= f_m(V, m).
\end{aligned}
\tag{1}
$$

Here, V represents the transmembrane voltage, $m \in \mathbb{R}^{15}$ represents a set of intracellular ion concentrations and gating variables responsible for determining the membrane current, I_{ext} represents the effect of an external pacemaker, and C_m is the membrane capacitance. Here, we use default model parameters from (61), with adjustable parameters taken to be $\tau_f = 70$ ms, $u = 9\text{s}^{-1}$, $\gamma = 0.4$, and $\bar{I}_{\text{NaCa}} = 8 \times 10^4 \mu\text{M}/s$, so that alternans develop as the pacing rate decreases. With this choice of parameters, alternans are driven by both voltage and calcium instabilities (in 1-D and 2-D simulations, we will choose parameters so that alternans are driven primarily by calcium instabilities). We analyze this model for pacing at different rates, where

$$
T_n \equiv \tau_n - \tau_{n-1} = \text{BCL} + \sigma \eta_n.
$$

Here, τ_n is the timing of the nth action potential, BCL is the nominal BCL, η_n is an independent random variable drawn from a standard normal distribution used to simulate variability in the timing of each depolarization, and $\sigma > 0$ is a constant that determines the magnitude of the variability. In simulations, gating variables are updated according to a Rush-Larsen (62) (cf. (63)) scheme in which all other variables are updated according to a forward-Euler scheme with a time step of 0.01 ms. In all single-cell simulations, data are recorded after 100 beats have elapsed to allow for transient effects from initial conditions to die out.

1-D and 2-D numerical simulations

For 1-D and 2-D numerical simulations, the following model is used:

$$
\begin{aligned}
C_m \frac{\partial V}{\partial t} &= D\Delta V - (I_{\text{ion}}(x, V, w) + I_{\text{ext}}(x, t)), \\
\frac{dw}{dt} &= f_m(x, V, w).
\end{aligned}
\tag{2}
$$

Here, $D = 1.6 \text{ cm}^2/\text{s}$ is the diffusion constant, x gives the spatial location on the domain, and Δ is the Laplacian. Ionic currents, I_{ion}, and auxiliary variables, $w \in \mathbb{R}^q$, are taken from the Fox-McHarg-Gilmour (FMG) model (64) and the Shiferaw-Fox model (61), where the number of variables, q, de-

pends on the model being used. In all models, nominal parameter sets are used except where noted otherwise, and the values of adjustable parameters are given in the Results.

The tissue is paced at location $x = \vec{0}$, where $\vec{0}$ is an appropriately sized vector of zeros with external current I_{ext}, so that the difference in successive depolarizations is given by

$$
T_n(\vec{0}) = \text{BCL} + \delta_n.
\tag{3}
$$

Here, $T_n(x)$ gives the time between successive depolarizations at location x, and δ_n is the deviation from the nominal BCL on the nth beat and is used to incorporate variance in the HR. For now, we take $\delta_n = \sigma \eta_n$, i.e., a zero mean Gaussian random variable with variance σ^2. Later, we will investigate possible modifications of δ_n to study the effects of feedback control on the pacing rate. In 1-D simulations, we use a 10-cm-long domain, with a 100 μm (200 μm) spatial discretization for the FMG model (Shiferaw-Fox model) with a numerically determined resting-space constant of 880 μm (860 μm).

In 2-D simulations, cellular dynamics are determined by the FMG model using the nominal parameter set from (64) unless otherwise stated. Simulations are performed on a 7cm×7cm sheet and discretized on a 500×500 grid. Previously, authors have investigated the dependence on the FMG model's behavior for various spatial discretizations (65). Results presented in this manuscript did not change qualitatively when using a 250 × 250 grid, suggesting that the spatial resolution is adequate. In 2-D simulations, τ_j is taken to be 1.11 times the nominal value from (64), resulting in a steepened CV restitution curve (cf. (34)). With this choice of parameters, the numerically determined resting-space constant for this model is 530 μm. During discordant alternans, nodal lines in 2-D simulations are calculated by subtracting the APD on successive beats and using the contour command in Matlab to find the zero level set.

In all 1-D and 2-D simulations, gating variables are updated according to a Rush-Larsen (62) (cf. (63)) scheme with all other variables updated according a forward-Euler scheme with a time step of 0.03 ms. In 1-D and 2-D simulations of the FMG model, initial conditions for $V, [\text{Ca}^{2+}]_i, [\text{Ca}^{2+}]_{\text{SR}}, f, d, m, h, j, f_{\text{Ca}}, X_{\text{Kr}}, X_{\text{Ks}}, X_{\text{to}}$, and Y_{to} at all locations are taken to be -87.5 mV, 0.159 μmol, 316.8 μmol, 0.723, 0.0001, 0.0010, 0.810, 0.348, 0.249, 0.480, 0.033, 0.0001, and 0.908, respectively. For all 1-D simulations of the Shiferaw-Fox model, initial conditions for $V, c_s, c_i, c_j, c_j', I_{\text{rel}}, d, f, q, m, h, j, X_{\text{Kr}}, X_{\text{Ks}}, X_{\text{to}}$, and Y_{to} are taken to be -95.9 mV, 0.673 μmol, 0.567 μmol, 138 μmol, 130 μmol, 0.0001 pA/pF, 0, 0.911, 0.515, 0.0002, 0.999, 0.919, 0.767, 0.031, 0, and 1, respectively. All 1-D and 2-D simulations are run for 300 beats before data are recorded to allow transient behavior to die out.

Quantifying severity of spatial dispersion of refractoriness caused by discordant alternans

Discordant alternans is characterized by the development of a spatial dispersion of refractoriness within cardiac tissue. As such, we will use the following metric to quantify the severity of dispersion in numerical simulations:

$$
\psi_n = \max_{x \in \mathcal{D}}(\|\nabla A_n(x)\|).
\tag{4}
$$

Here, x represents a spatial location on the domain $\mathcal{D}$, $A_n(x)$ is the APD at location x on the nth beat, where the APD is calculated as the time required to reach 90% repolarization, ∇ denotes the gradient, and double vertical lines indicate the Euclidian (i.e., L^2) norm. With these definitions, ψ_n provides an estimate for the maximal local dispersion in APDs, with larger values corresponding to more severe dispersion. We emphasize that discordant alternans is not the only phenomenon that can cause spatial differences in APDs. For instance, variation in the properties of epicardial and endocardial cells can result in spatial gradients in APD throughout the heart (66). Additionally, heterogeneity in electrotonic effects due to tissue shape and

pacing location can also induce significant APD dispersion ([67–69]). Nevertheless, in this work, large values of Eq. 4 correspond to discordant alternans, whereas small values are observed only during concordant alternans (see Fig. 1, A–C, for an example of Eq. 4 plotted against the spatial APD profile on a 1-D domain).

Note that although alternans is characterized by the beat-to-beat variation in electrochemical dynamics, the dispersion of refractoriness resulting from discordant alternans promotes the development of further reentrant arrhythmia; the metric from Eq. 4 characterizes the severity of the latter. In 1-D simulations, we exclude values within 2 cm of the boundary in the calculation of Eq. 4, because these locations have a tendency to differ from the rest of the tissue regardless of whether alternans is concordant or discordant (cf. ([67])). Likewise, in 2-D simulations, we exclude locations within 1 cm of the tissue boundary. This decision does not qualitatively change the results presented in this work.

Fitting computational data to simplified single-cell dynamics

In single-cell simulations, it is useful to analyze Eq. 1 in terms of the simplified map (cf. ([41,70,71])):

$$
\begin{aligned}
A_{n+1} &= f(D_n) + \xi(C_{n+1}), \\
C_{n+1} &= \rho(D_n) - g(C_n), \\
D_n &= \mathrm{BCL} + \sigma\eta_n - A_n.
\end{aligned}
\tag{5}
$$

Here, A_n and D_n represent a cell's nth APD and diastolic interval (DI), respectively, C_n is the peak of the intracellular calcium concentration on the nth beat, and f, g, ξ, and ρ are functions that determine the relationship between APD and calcium dynamics. The function $f(D_n)$ incorporates the effects of all noncalcium ionic currents and is generally a monotonically increasing function. Likewise, ρ increases monotonically due to graded calcium release ([72,73]). The function ξ reflects the direction of calcium-APD coupling and can be either positive or negative depending on whether alternans is electromechanically concordant or discordant ([61]), and the slope of g determines the stability of the voltage-clamped calcium dynamics.

To fit the model described by Eq. 1 to the simplified map (Eq. 5), we suppose that $A^* = f(D^*) + \xi(C^*)$ and $C^* = \rho(D^*) - g(C^*)$, and that $D^* = BCL - A^*$ is a fixed point solution of mapping Eq. 5 when $\sigma = 0$; manipulation of Eq. 5 and linearization around this fixed point yields the relation

$$
\begin{bmatrix} \Delta A_{n+1} \\ \Delta C_{n+1} \end{bmatrix} = \begin{bmatrix} f' + \xi'\rho' & -\xi' g' \\ \rho' & -g' \end{bmatrix} \begin{bmatrix} \Delta D_n \\ \Delta C_n \end{bmatrix},
\tag{6}
$$

where $\Delta A_n = A_n - A^*$, $\Delta D_n = D_n - D^*$, $\Delta C_n = C_n - A^*$, and the prime symbol denotes the derivative evaluated at the fixed point. Suppose that we have the ability to take multiple measurements of A_n, C_n, and D_n to construct an overdetermined matrix equation,

$$
\begin{bmatrix} \Delta A_1 & \Delta A_2 & \dots & \Delta A_N \\ \Delta C_1 & \Delta C_2 & \dots & \Delta C_N \end{bmatrix} = \begin{bmatrix} p_{11} & p_{12} \\ p_{21} & p_{22} \end{bmatrix} \times \begin{bmatrix} \Delta D_0 & \Delta A_1 & \dots & \Delta A_{N-1} \\ \Delta C_0 & \Delta C_1 & \dots & \Delta C_{N-1} \end{bmatrix},
\tag{7}
$$

where each column of the left and right matrices corresponds to the measurements taken on a single beat, and the 2×2 matrix corresponds to the unknown matrix of derivatives from Eq. 6. Note that the stochastic term from Eq. 5 is absorbed into the measurements of the DI in Eq. 7. The above equation can be written as a standard system of linear equations,

$$
\begin{bmatrix} \Delta A_1 \\ \Delta C_1 \\ \vdots \\ \Delta A_N \\ \Delta C_N \end{bmatrix} = \begin{bmatrix} \Delta D_0 & \Delta C_0 & 0 & 0 \\ 0 & 0 & \Delta D_0 & \Delta C_0 \\ & & \vdots & \\ \Delta D_{N-1} & \Delta C_{N-1} & 0 & 0 \\ 0 & 0 & \Delta D_{N-1} & \Delta C_{N-1} \end{bmatrix}
$$
$$
\times \begin{bmatrix} p_{11} \\ p_{12} \\ p_{21} \\ p_{22} \end{bmatrix},
\tag{8}
$$

for which a least-squares estimate for the unknown coefficients can be obtained by taking the pseudoinverse of the large matrix ([74]). Using these four coefficients, estimates of each of the four derivatives that make up the 2×2 matrix in Eq. 6 are straightforward to obtain.

RESULTS

Stochastic pacing inhibits discordant alternans in 1-D simulations

We investigate the relationship between stochastic pacing and alternans on a 1-D domain with simulations of Eq. 2, where δ_n is drawn from a zero-mean Gaussian distribution with variance σ^2. We consider the case where the development of alternans is mediated primarily by steep APD restitution and use the FMG model ([64]) to characterize the cellular ionic dynamics I_{ion}. Here, calcium dynamics follow passively; attention will also be given shortly to the case where alternans is driven by calcium instabilities.

Equation 2 is simulated for different values of σ and BCL. In the results to follow, when BCL = 185 and 190, τ_j, the slow inactivation variable of the sodium current, is taken to be 1.25 times its nominal value to steepen CV restitution so as to produce discordant alternans (cf. ([34])). In simulations presented here, the maximal value of σ is ~5% of the nominal BCL. In each of these simulations, when σ is small, discordant alternans develops, as shown in Fig. 1 A. During discordant alternans, a node develops, i.e., a location for which the APD is identical on a beat-to-beat basis. Due to stochastic pacing, the node moves throughout the medium and on occasion will disappear if it travels too close to the paced end, briefly producing a pattern of concordant alternans (see Fig. 1 B). In simulations with BCLs of 180, 185, and 190 ms without stochastic pacing, a stable, stationary node forms in the steady state.

When σ is small, discordant alternans persists throughout most of the simulation, as shown in Fig. 1 C. For larger values of σ, discordant alternans can still form, but it does not last long before disappearing, resulting in smaller values of ψ_n overall, as seen in Fig. 1 D. Fig. 1 E shows $\overline{\psi}_n$, the mean value of ψ_n after transient behavior is allowed to decay. This value is normalized by the maximal value of $\overline{\psi}_n$ obtained for each BCL to make comparisons between trials. The value of $\max(\overline{\psi}_n)$ is equal to 28, 22, and 15 ms/cm for BCLs of 180, 185, and 190 ms, respectively. Each data

point is obtained using 4000 beats for the given set of parameters; statistical independence is assumed after 30 beats, and samples are taken at this interval to calculate the mean and SE. We note that when BCL = 180 ms, conduction block occasionally occurs at the pacing site no more than once in every 400 beats on average due to the large magnitude of alternans. For $\sigma > 8$, conduction block occurs more frequently, and we do not include these data points in Fig. 1 E. In general, once σ crosses a certain threshold, the variability starts to suppress discordant alternans. Furthermore, this threshold increases as ψ_n grows; when BCL = 190 ms, $\sigma = 2$ ms begins to suppress discordant alternans, whereas when BCL = 180 ms, $\sigma = 4$ ms is required before ψ_n starts to decrease.

In simulations from Fig. 1, alternans is caused by steep APD restitution, so that calcium dynamics follow passively from the voltage dynamics. However, alternans in living tissue is most likely due to the coupling between calcium and voltage restitution dynamics (39). Here, we also investigate the formation and maintenance of discordant alternans when the cellular alternans can be attributed to instabilities in the calcium dynamics by simulating Eq. 2 with ionic dynamics that are given by the Shiferaw-Fox model (61). Adjustable parameters from the Shiferaw-Fox model are taken to be $\tau_f = 30$ ms, $u = 9\text{s}^{-1}$, and $\bar{I}_{\text{NaCa}} = 4 \times 10^4 \mu\text{M}/s$. As explained in (61), parameters τ_f and u determine the propensity for voltage and calcium alternans, respectively, and these parameters are chosen so that the resulting alternans are primarily mediated by calcium instabilities. In 1-D simulations of the Shiferaw-Fox model, τ_j is taken to be seven times its nominal value, so that CV restitution is steepened, allowing discordant alternans to form. We focus on combinations of parameters for which alternans is electromechanically concordant, i.e., with long (short) action potentials corresponding to large (small) calcium transients, which are commonly observed in experiments (37,46,75) and tend to produce alternans of larger magnitude. The BCL is taken to be 310 ms, and different values of γ are used to

manipulate the severity of dispersion caused by discordant alternans. We decrease γ rather than decreasing the BCL to make conduction block less common for larger values of σ. In simulations with these parameters, in the absence of stochastic pacing, a stable, stationary node forms in the steady state. In Fig. 2, the maximal value of σ is ~8% of the nominal BCL. During simulations with large σ, the system switches between concordant and discordant alternans, as shown in Fig. 2, A and B. As seen in Fig. 2, C and D, a pattern similar to the previous simulations emerges: as the magnitude of σ increases, $\overline{\psi}_n$ is significantly diminished. For larger values of σ, conduction block occurs at the pacing site less than once every 1000 beats. Conduction block is not observed when $\sigma \leq 20$ ms.

In simulations from Figs. 1 and 2, we observe that incorporating stochastic pacing inhibits the formation of discordant alternans as the variance increases. In these simulations, without stochastic pacing, a stable, stationary node forms in the steady state. Simulations in Fig. 3 investigate the effect of stochastic pacing when corresponding deterministic simulations do not display discordant alternans in the steady state. Fig. 3 A shows results for the FMG model where, as in other simulations, τ_j is multiplied by 1.25 times its nominal value from (64) to steepen the CV restitution curve. All other parameters are identical to those from Fig. 1. Fig. 3 B shows results for the Shiferaw-Fox model, where $\gamma = 0.60$ and all other parameters are identical to those used for simulations in Fig. 2. In each trial, ψ_n is taken over 3500 consecutive beats after transient behavior has been allowed to decay, and the mean ± SE values of ψ_n are computed using the same procedure as in Figs. 1 and 2. In Fig. 3 A and B, discordant alternans forms when $\sigma = 0$ and the BCL is 190 ms (-310 and 330 ms). In these simulations, stochastic pacing reduces the value of $\overline{\psi}_n$ to approximately one third of its value from corresponding deterministic simulations. When $\overline{\psi}_n$ is small during deterministic simulations (i.e., with discordant alternans not present) it remains small in trials with stochastic pacing.
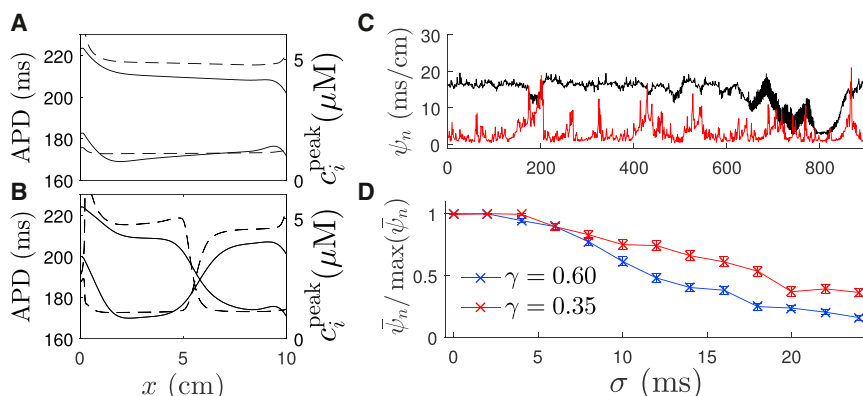

FIGURE 2 (A and B) Example of concordant (A) and discordant (B) APDs and calcium dynamics. Solid lines represent the APDs on successive beats and dashed lines give the peak value of the intracellular concentration on successive beats. (C) ψ_n as a function of beat number for simulations with $\gamma = 0.6$ for $\sigma = 20$ ms (red trace) and $\sigma = 4$ ms (black trace). In simulations where the variance of the stochastic pacing is larger, the system spends a majority of its time in a concordant alternans state, as reflected in lower values of ψ_n. (D) Mean, $\overline{\psi}_n$, and SE calculated over simulations of >4000 beats for each set of parameters. Statistical independence is assumed after 60 beats, and measurements are taken at this interval to calculate the mean ± SE. The value of max($\overline{\psi}_n$) is equal to 17 and 24 ms/cm in simulations where $\gamma = 0.6$ and 0.35, respectively. To see this figure in color, go online.
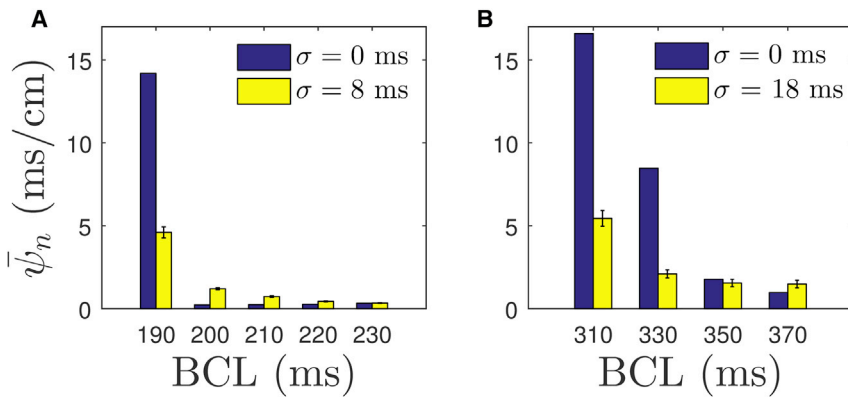
FIGURE 3 Simulations of the FMG model (*A*) and the Shiferaw-Fox model (*B*) with and without stochastic pacing. Discordant alternans develops when $\sigma = 0$ for BCLs of 190 ms (*A*) and 310 and 330 ms (*B*). At these BCLs, stochastic pacing significantly reduces the occurrence of discordant alternans. Furthermore, it does not promote discordant alternans when corresponding deterministic simulations do not exhibit discordant alternans. To see this figure in color, go online.

Results presented in Figs. 1, 2, and 3 suggest that stochastic pacing rates might be antiarrhythmic by inhibiting the formation of discordant alternans. The sections to follow will be devoted to understanding the mechanism by which stochastic pacing causes this behavior. We will analyze alternans in both single-cell models of cardiac action potentials and models in one and two spatial dimensions.

Analysis of stochastic pacing in single cardiomyocytes

Cardiac alternans manifests at a cellular level as a result of instabilities due to a period of doubling bifurcation resulting from the interplay between cellular calcium dynamics and APD restitution (37,39,76,77). Here, we investigate the formation of alternans in Eq. 1 in the presence of stochastic pacing.

Fig. 4 *A* shows the voltage and intracellular calcium concentration for the Shiferaw-Fox model at successive beat numbers in a simulation where $\sigma = 10$ ms and the BCL is 390 ms. Model parameters are given in the Methods. Here, the calcium cycling is in phase with alternating calcium dynamics leading to alternating long and short action potentials. Fig. 4 *B* shows the bifurcation diagrams of the APD when $\sigma = 0$; stable alternans solutions form at a BCL of ~440 ms. In single-cell simulations, the APD is

calculated as the time required to reach 95% repolarization. In the deterministic case (i.e., with $\sigma = 0$), the alternans amplitude represented by $|A_{n+1} - A_n|$ approaches the solid black line in Fig. 4 *C*, which is the difference between the top and bottom curves in Fig. 4 *B* (and simply zero when the period-1 solution is stable). When we include variability in the action potential timing, alternans can develop even when the underlying period-1 dynamics are stable. The crosses in Fig. 4 *C* represent the mean value, and the vertical bars contain 80% of the values in alternans severity with $\sigma = 10$ ms (~2.5% of the BCL). In these simulations, variability promotes the development of alternans near the bifurcation and has little effect farther away. Similar behavior has also been observed previously (58,59).

To provide a theoretical underpinning of the behavior observed here, we analyze the simplified dynamical map (Eq. 5). In Appendix A, we show that when the underlying period-1 (i.e., alternans-free) behavior is stable, variance in APDs, denoted by ν_∞, is directly proportional to the variance in the DI, σ. Furthermore, by estimating the values of $f' \equiv \frac{\partial f}{\partial D_n}\Big|_{D^*}$, $\rho' \equiv \frac{\partial \rho}{\partial D_n}\Big|_{D^*}$, $g' \equiv \frac{\partial g}{\partial C_n}\Big|_{C^*}$, and $\xi' \equiv \frac{\partial \xi}{\partial C_n}\Big|_{C^*}$, where D^* and C^* correspond to the steady-state DI and maximal calcium concentration, respectively, this proportionality constant can be calculated exactly. For example, Eq. 1 is simulated with a BCL of 450 and $\sigma = 2$ ms. All
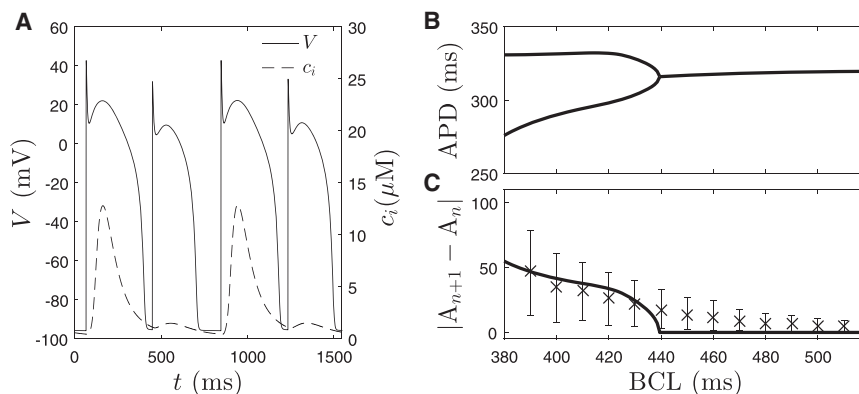

FIGURE 4 (*A*) Relationship between the alternant calcium and voltage behavior in simulations of Eq. 1 with BCL = 390. (*B*) Period doubling bifurcation as the BCL changes. (*C*) Alternans amplitude in simulations with stochastic pacing. The solid line represents the value when $\sigma = 0$ and is determined by the vertical distance between the curves from (*B*). For $\sigma = 10$ ms, 2000 beats are simulated at each BCL, with 80% of recorded values contained within the vertical bars. Crosses give the mean value in these simulations.

data are taken after the initial transient behavior dies out. Values of A_n and C_n are recorded for each action potential, and f', g', ξ', and ρ' are found to be 0.11, 0.66, 3.47, and 0.074, respectively, from a least-squares fit to the data, as detailed in Fitting Computational Data to Simplified Single-Cell Dynamics. The resulting variance in the APDs is calculated to be $v_\infty = 4.5\sigma^2$ from Eq. A8. The same procedure is repeated for BCL = 550 ms, and the values of f', g', ξ', and ρ' are determined to be 0.03, 0.55, 2.73, and 0.043, respectively, after fitting to the data, yielding $v_\infty = 0.11\sigma^2$. Histograms in Fig. 5, *left*, show the alternans amplitude, with red lines representing the predicted normal distribution based on the corresponding value of v_∞ with near perfect agreement. Fig. 5 (*right*) gives values of v_∞/σ^2 as a function of the different parameters. Dashed and solid lines correspond to $\log_{10}(v_\infty/\sigma^2) = 0$ and 1 level sets, respectively. White corresponds to locations for which the period-1 solution is unstable (i.e., alternans is stable), so that v_∞ cannot be calculated using Eq. A8. The boundary between yellow and white regions represents the period-doubling bifurcation for which the period-1 solution loses stability to the period-2 alternans solution. As parameters change so that they are closer to the bifurcation, the effect of stochastic pacing is amplified, yielding severe alternans even for relatively small values of σ. Conversely, parameter sets farther from the bifurcation tend to absorb the stochastic effects, leading to small variations in the measured APDs. These results are consistent with the observation that HR variation can lead to the onset of alternans, as even small variations in pulse timing can produce large excursions from the period-1 alternans free dynamics. The effect of calcium cycling on the APD tends to have a significant effect on the variance of APDs. In Fig. 5 (*right*), larger coupling be-

tween the calcium cycling and APDs (resulting in larger values of ξ') tends to promote instabilities in the alternans dynamics. Conversely, when ξ' is small (as is the case in the Fig. 5, *bottom right*), the variance remains relatively low until either f' or g' approach 1. Similar analysis could be performed in the case where the period-2 alternans dynamics are stable by analyzing the associated stable period-2 map.

Variance in the timing of depolarizations of a single cardiomyocyte leads directly to variance in the APDs, which can be predicted precisely according to Eq. A8. These results could lead to the interpretation that HRV promotes alternans, possibly promoting further and more serious arrhythmias such as tachycardia and fibrillation. However, analysis of alternans in single cells cannot account for spatial dispersion of refractoriness, which develops during discordant alternans and is widely regarded to be a precursor to more lethal cardiac arrhythmias. In the sections to follow, we investigate the dynamical behavior of discordant alternans in the presence of stochastic pacing.

Relationship between 1-D nodal dynamics and stochastic pacing

Results of simulations in Figs. 1 and 2 suggest that HRV could be antiarrhythmic in 1-D tissue, as it has a tendency to inhibit the formation and maintenance of discordant alternans. Insight into the mechanism by which variability suppresses discordant alternans can be gained by investigating nodal dynamics during discordant alternans, i.e., the location x_n^*, for which $A_n(x_n^*) = A_{n-1}(x_n^*)$. To make analysis more tractable, we will consider the case in which alternans
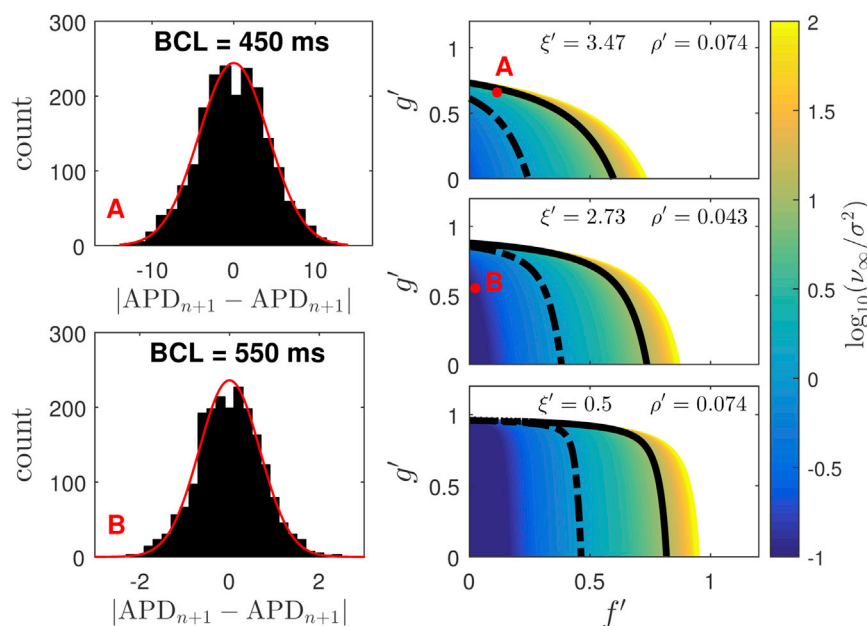

FIGURE 5 Histograms on the left (*A* and *B*) represent simulated data with different BCLs and $\sigma = 2$ ms. Predicted normal distributions in red are calculated from Eq. A8 and are in near perfect agreement. Plots on the right show v_∞/σ^2 calculated according to Eq. A8 for parameters from the linearized Eq. A2, with solid and dashed black lines corresponding to level sets equal to 1 and 0, respectively. Points labeled A and B correspond to the parameters that give the best fit from simulations with BCL = 450 and 550, respectively. To see this figure in color, go online.

is caused by steep APD restitution with calcium dynamics following passively. Later sections will be devoted to understanding systems for which alternans is caused by instabilities in the intracellular calcium dynamics, as is the case for the results in Fig. 2.

Looking closely at how x_n^* changes in Fig. 6 (*upper*), when $\sigma = 1$ ms, the node travels between 4.2 and 5 cm with dynamics that resemble a mean-reverting stochastic process (78). When $\sigma = 5$ ms, the excursions from the mean are larger, and occasionally, the node is eliminated by passage through the paced end of the tissue. When the node is eliminated, the behavior temporarily reverts to concordant alternans. Recalling the results from of Fig. 1 E, the dispersion of APDs is larger on average when σ is smaller, as it takes a nonnegligible amount of time for discordant alternans to redevelop from the concordant state.

For fixed pacing rates, nodal dynamics of discordant alternans can be analyzed in the limit that the cellular dynamics are close to the period-doubling bifurcation (40,79). In this case, the APD dynamics are assumed to change slowly enough on a beat-to-beat basis that they can be approximated with a continuous-time partial differential equation. Here, variable pacing rates invalidate these assumptions, and a different approach is necessary. The derivation to follow gives a relation for the change in node position $x_{n+1}^* - x_n^*$ due to perturbations to the nominal BCL, as shown, for example, in Fig. 6 (*lower*).

To begin, for alternans driven by voltage instabilities, the APD is a function of the DI (36), electrotonic effects of coupling between cells (35), and memory effects due to pacing history (80,81). To simplify the analysis, we will assume that variations in the pacing rate are small enough that mem-ory effects are negligible, and the APD dynamics are given by (cf. (35,40,79))

$$A_{n+1}(x) = f(D_n(x)) + \alpha_n(x), \qquad (9)$$

where $f(D_n(x))$ gives the relationship between the DI and the APD, and $\alpha_n(x)$ accounts for electrotonic effects on the nth beat. The DI can be related to the APD through the relation

$$D_n(x) = T_n(x) - A_n(x), \qquad (10)$$

where $T_n(x)$ is the difference between the timing of successive depolarizations, $\tau_n(x)$ and $\tau_{n-1}(x)$. When the pacing occurs at $x = 0$, $T_n(x)$ can be calculated according to

$$
\begin{aligned}
T_n(x) &\equiv \tau_n(x) - \tau_{n-1}(x) \\
&= \left(\tau_{n-1}^* + \text{BCL} + \delta_n + \int_0^x \frac{dx'}{c(D_n(x'))} \right) \\
&\quad - \left(\tau_{n-1}^* + \int_0^x \frac{dx'}{c(D_{n-1}(x'))} \right) \\
&= \text{BCL} + \delta_n + \int_0^x \left(\frac{1}{c(D_n(x'))} - \frac{1}{c(D_{n-1}(x'))} \right) dx'.
\end{aligned}
$$
$$(11)$$

Here, τ_n^* gives the time at which a new pulse is applied at the pacing site, δ_n is some variation from the nominal BCL, and $c(D_n(x))$ describes CV restitution, i.e., the speed of the excitable wave front as a function of the DI.

In Appendix B, using Eqs. 9, 10, and 11 as a starting point, we derive the following relation to predict
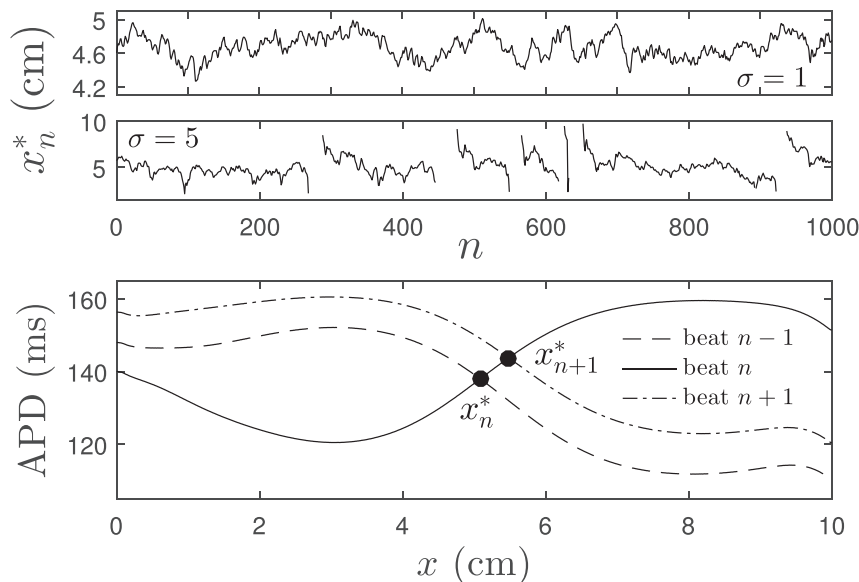

FIGURE 6 The top two plots show the nodal dynamics in simulations of Eq. 2 with BCL = 185 ms and two different values of σ. When $\sigma = 1$ ms, the dynamics are reminiscent of a mean reverting stochastic process. For $\sigma = 5$ ms, the node occasionally escapes through the paced end of the tissue resulting temporarily in concordant alternans (which does not have a node). The bottom plot gives an example of the APD on successive beats from simulations with $\sigma = 5$ ms.

how the node location changes as a function of the previous DIs:

$$x_{n+1}^* - x_n^* = \frac{1}{\phi_n}\left[\delta_n - \delta_{n-1} + \frac{\alpha_n(x_{n+1}^*) - \alpha_{n-1}(x_{n+1}^*)}{f'|_{D_{n-2}(x_{n+1}^*)}}\right.$$
$$\left. + \Lambda_n(x_{n+1}^*)\right]. \quad (12)$$

Here, $\phi_n \equiv (\partial A_n/\partial x - \partial A_{n-1}/\partial x)$ evaluated at x_n^* (i.e., the slope of the alternans profile evaluated at the node) and $\Lambda_n(x_{n+1}^*)$ account for CV restitution effects, as defined in Eq. B4 of Appendix B. Equation 12 is a complicated, implicit equation describing the nodal movement as a function of the previous two perturbations to the nominal cycle length. However, in the analysis to follow, we use a number of simplifications to further manipulate and understand the perturbed dynamics.

We analyze the system under conditions for which the deterministic system (i.e., with a fixed pacing rate) has a stable discordant alternans solution with a single node to simplify Eq. 12. First, consider the term ϕ_n from Eq. 12, the difference in slopes of the APD profile at the node. Fig. 7 B shows this value measured during 3900 beats in simulations of Eq. 2 using the FMG model for cellular dynamics with $\sigma = 2$ ms and BCL $= 185$ ms. We find that regardless of the node position, the magnitude of ϕ_n is nearly identical on a beat-to-beat basis and changes sign depending on whether the APD profile is increasing or decreasing at the node (as shown, for example, in the dashed and solid profiles, respec-

tively, in Fig. 6 (lower)). Based on this, we made the following approximation to simplify Eq. 12:

$$\partial_x A_n - \partial_x A_{n-1} = \phi_n \approx (-1)^n \beta, \quad (13)$$

where $\beta \in \mathbb{R}$ and the alternating sign results from the alternating long and short action potentials. Intuitively, this behavior tends to occur because premature (delayed) beats cause the entire APD profile to fall (rise), but do not have much overall effect on the shape.

Next, we consider the term $(\alpha_n(x_{n+1}^*) - \alpha_{n-1}(x_{n+1}^*))/f'|_{D_{n-2}(x_{n+1}^*)}$ from Eq. 12, which represents the electrotonic effects on the APD on successive beats. These electrotonic effects are responsible for a pronounced shift between dynamic restitution curves on alternating beats (35,79). In simulations with stochastic pacing, Fig. 7 C shows the APD as a function of the DI, with data points taken within 3 mm of the node. Because the times between successive depolarizations are similar enough that memory effects are negligible, the approximately constant vertical shift between each set of data points is mostly due to electrotonic effects. For this reason, we approximate the magnitude of $\alpha_n(x_{n+1}^*) - \alpha_{n-1}(x_{n+1}^*)$ by a constant. Furthermore, the slope of these restitution curves is also nearly constant near the node. Taken together, this yields the approximation

$$\frac{\alpha_n(x_{n+1}^*) - \alpha_{n-1}(x_{n+1}^*)}{f'|_{D_n(x_{n+1}^*)}} \approx (-1)^n J, \quad (14)$$
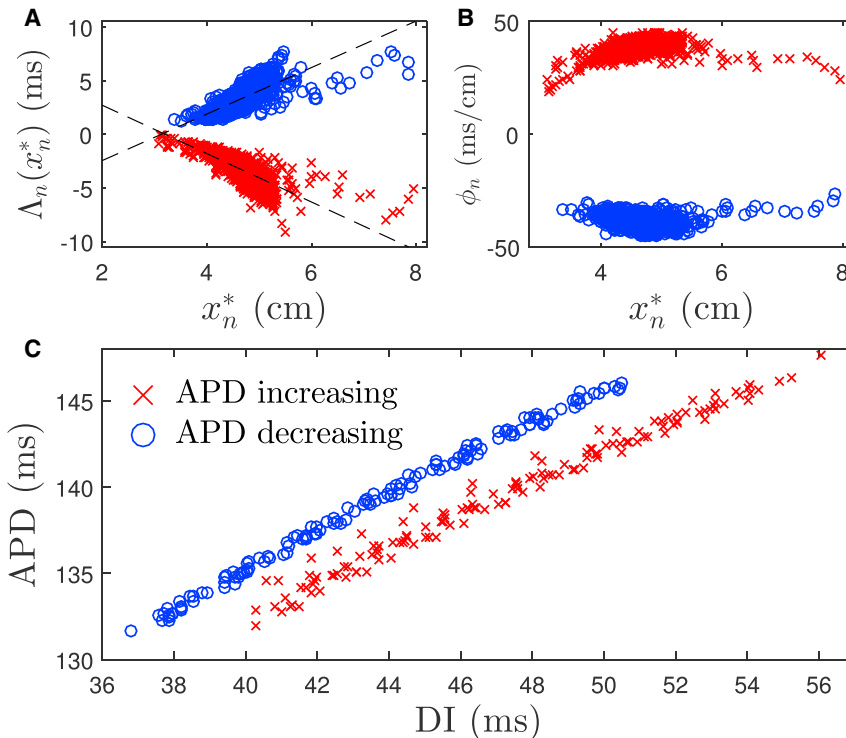
where J is a constant.

FIGURE 7 Illustration of simplifying assumptions used in (53) in simulations of Eq. 2 using the FMG model for the cellular dynamics with BCL $=$ 185 ms and $\sigma = 2$ ms. Blue circles and red crosses represent data points taken when the APD profile is decreasing and increasing, respectively, at the node location. (A) Cycle length at the node varies linearly with its spatial location to a reasonable approximation. This linear approximation can be used to estimate k from Eq. 15. (B) The magnitude of ϕ_n is approximately constant on each beat, providing an estimate for β from Eq. 13. Notice that $\Lambda_n(x_n^*)$ and ϕ_n have opposite signs, so that $k\beta < 0$. (C) The dynamic restitution curve shifts in an alternating pattern and can be used to approximate the effect of electrotonic coupling from Eq. 12. To see this figure in color, go online.

Finally, authors (35) have noted previously that differences in cycle length due to CV restitution can be approximated by considering the difference between the maximal and minimal CV during discordant alternans. Such an approximation gives a linear relationship between the node location and the difference in cycle length. Here, we take a similar approach. Starting with Eq. 11, one can show that $\Lambda_n(x_n^*) = T_n(x_n^*) - T_{n-1}(x_n^*) - \delta_n + \delta_{n-1}$. Using this relation, in Fig. 7 A, when we plot $\Lambda_n(x_n^*)$ over the course of a simulation of Eq. 2, a linear relationship emerges that alternates on a beat-to-beat basis. Therefore, we make the approximation

$$\Lambda_n\left(x_n^*\right) \approx (-1)^n \left[a + k x_n^*\right], \tag{15}$$

where a and k are determined from linear fits to the data, for example, in Fig. 7 A. Using the relations of Eqs. 13–15, and modeling HRV with a series of normally distributed random perturbations (i.e., $\delta_n = \sigma \eta_n$, with η_n taken from a standard normal distribution and $\sigma > 0$), Eq. 12 is greatly simplified, which allows for further analysis. Specifically, as we show in Appendix C, in the limit as n approaches infinity, the average node location is equal to $(J + a)/k$, with a variance given by

$$v_\infty = \frac{-2\sigma^2}{k\beta - k^2}. \tag{16}$$

Note here that $k\beta < 0$, as explained in Appendix C. Equation 16 states that given enough time to forget initial conditions, the variance of the node location is proportional to the square of variance of stochastic pacing and inversely related to both the slope of the alternans profiles, β, and the linear relationship between the cycle length and the node location, k.

Fig. 8 shows results of simulations testing the accuracy of predictions on the mean and variance of the node location for simulations of Eq. 2 using the FMG model for the cellular dynamics with BCL = 185 ms and various values of σ. For each simulation, the parameters β, J, k, and a from Eqs. 13, 14, and 15 are estimated from simulation data (e.g., using measurements similar to those shown in Fig. 7). Overall, the mean is accurate to within 0.05 cm and the distribution is well predicted by the Gaussian. In each of these simulations, the tail of the distribution near the paced end of the domain is slightly longer than would be expected from a normal distribution. This behavior could be explained by examining the data in Fig. 7: as x_n^* approaches the paced end at $x = 0$, the slope of the relation for Λ_n starts to flatten, and the values of ϕ_n tend to curl toward zero. Both of these effects cause the node to be pulled less strongly toward the center of the tissue and allow it to escape more easily through the paced end.

Qualitatively, the alternans behavior from Fig. 1 can be interpreted in terms of the escape time from a potential well. As Fig. 9 illustrates, discordant alternans nodes tend to form opposite the paced end of the tissue. Without stochastic pacing, the node makes its way to a steady-state location, x_{fp}. For small values of σ, it is unlikely for the node to travel far from its mean value, allowing discordant alternans to persist. As the magnitude of the variability increases, larger excursions from the mean are more likely, lowering the average time required for the node to be absorbed by the paced end. Although the node eventually returns, if variability is large enough, it will not persist for very long, resulting in mostly concordant alternans. This behavior represents a possible mechanism by which HRV provides protection from the stable formation of discordant
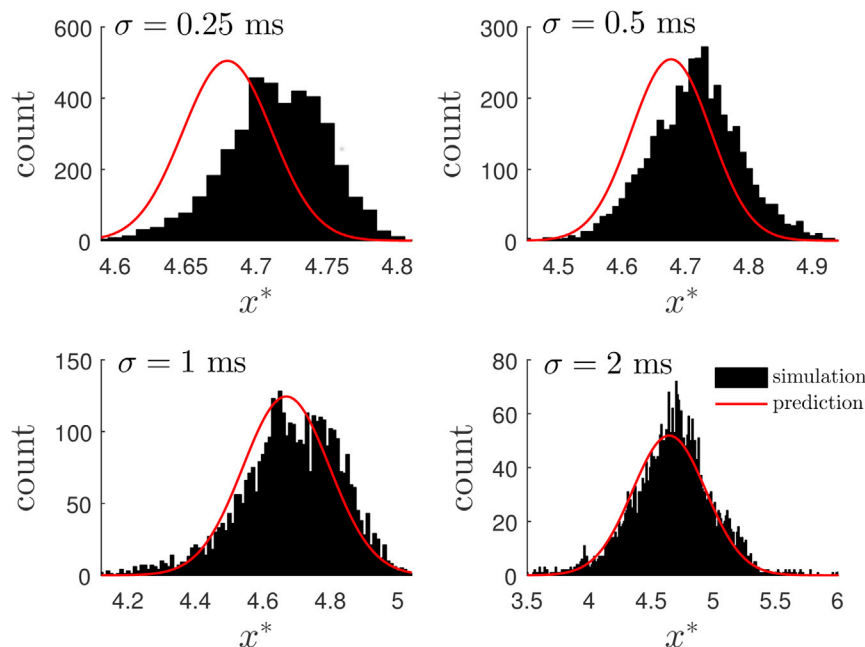

FIGURE 8 Results of simulations of Eq. 2 over 4000 APDs. On each beat, the node location is calculated and data are represented with a histogram. A red Gaussian curve is shown with mean and variance estimated according to the simplified dynamics (Eq. 16). The prediction of the mean value of x^* is within ~0.05 cm (note that the scale on the bottom axis is different in each plot). To see this figure in color, go online.
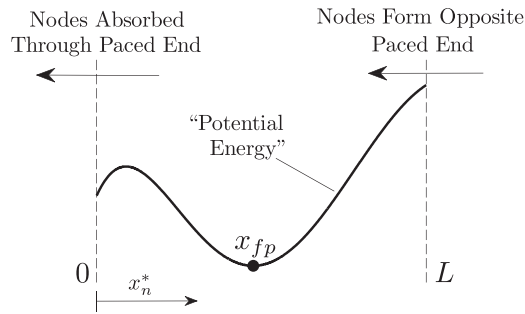
FIGURE 9 Alternans behavior interpreted as escape from a potential well. Equation 16 illustrates that the variance of x_n^* near x_{fp} is proportional to σ^2, the variance of the stochastic pacing rate. As σ grows, discordant alternans nodes are more quickly absorbed through the paced end of the tissue. In all 1-D and 2-D simulations in this work, parameters are chosen so that the concordant alternans pattern is not stable; nodes re-form opposite the paced end and rarely escape through this end.

alternans, making the development of reentrant arrhythmia less likely.

Cycle-length manipulation to eliminate discordant alternans

In the previous sections, we showed how stochastic pacing could discourage the formation of stable discordant alternans solutions. Here, we investigate a strategy for direct manipulation of the paced cycle length to further suppress the formation of alternans. In previous studies, authors have developed strategies that attempt to eliminate cardiac alternans through stabilization of the unstable period-1 behavior (82–84), thereby eliminating alternans entirely. However, such control strategies generally require control to be applied in multiple locations throughout the tissue when the magnitude of alternans or the domain is large (85). Here, we investigate a different approach, attempting to suppress discordant alternans to promote concordant alternans.

Previous analytical studies (40,79) have revealed that discordant alternans nodes tend to form opposite the paced end in 1-D tissue and travel toward the paced end. The node continues to travel until either electrotonic and CV restitution effects are balanced, forming a stable discordant alternans solution, or the node is absorbed through the paced end. Such behavior is qualitatively similar to simulations with stochastic pacing from the previous sections. For instance, in Fig. 6 (*middle*), nodes generally form opposite the paced end, travel randomly throughout the 1-D tissue, and eventually are absorbed by the paced end of the tissue.

The control strategy below exploits this behavior, hastening the destruction of the discordant alternans node, yielding alternans that is concordant for a majority of the time. We will assume that we have the ability to give a premature stimulus, but cannot delay the timing of a pulse. With this restriction, we can modulate stimulus timing so that

$$\delta_n = \min(\sigma \eta_n, \delta_n^c),$$

where δ_n^c is a control target. Recall from Eq. 11 that δ_n is the deviation from the nominal paced cycle length, so that $\delta_n < 0$ yields a premature pulse, whereas $\delta_n > 0$ results in a delayed pulse. The above equation assumes that in the absence of cycle-length manipulation, pacing rates are drawn from a Gaussian distribution with variance σ^2. The control will only modify the pulse timing if $\delta_n^c < \sigma \eta_n$.

With these constraints, as shown in Appendix D, assuming that only one node forms during discordant alternans, we can implement the following control strategy to drive the node to the tissue boundary:

$$\delta_n^c = \begin{cases} -\omega, & \text{if } A_n(x_1) - A_n(x_2) < -A_T, \\ \infty, & \text{otherwise,} \end{cases} \quad (17)$$

where $\omega > |kx_{fp}|$. This control strategy requires the placement of control electrodes at either end of the tissue at locations $0 \leq x_1 < x_2$ to measure successive APDs. Here $A_T > 0$ is some threshold used to trigger the control. Fig. 10 A, *upper* and *lower*, describes the setup of the control strategy described in Eq. 17, where two recording electrodes monitor action potentials to determine whether to elicit a premature stimulus. The requirement for the magnitude of ω is a conservative estimate based on the minimal amount of perturbation required to ensure that the node is driven to the tissue boundary. Note that choosing $x_1 = 0$ would require an electrode that can simultaneously record APDs and stimulate with a premature pulse. Intuitively, the control strategy (Eq. 17) works by delivering a premature stimulus at an appropriate time to actively drive a discordant alternans node to the tissue boundary to restore concordant alternans. At this point, the controller remains inactive until it detects the return of discordant alternans (setting $\delta_n^c = \infty$ is equivalent to turning the controller off).

To implement Eq. 17 in Eq. 2 using the FMG model for the cellular dynamics, we take $A_T = 20$ ms, $\omega = 10$ ms, $x_1 = 1$ cm and $x_2 = 9$ cm. In simulations, other placements of the control nodes work equally well provided they are placed sufficiently far apart to detect discordant alternans. Fig. 10 D shows the maximal value of the gradient in APDs as defined in Eq. 4 when $\sigma = 2$ ms and BCL $= 185$ ms with (*red lines*) and without (*black lines*) the control strategy (Eq. 17) applied. For these model parameters, $|kx_{fp}^*| \approx 10 = \omega$, so that the magnitude of the perturbations is expected to be sufficient to drive the node to the paced end. Once the control is engaged, the node is quickly driven to the paced end, restoring concordant alternans until the next node forms. This strategy gives the appearance of peaks in ψ_n occurring with a period of ~40 beats. Compared with the behavior of the uncontrolled system, the noise infrequently drives the node to the paced end so that alternans is primarily discordant, as reflected in larger values of ψ_n. Fig. 10, B and C, gives a comparison of the average
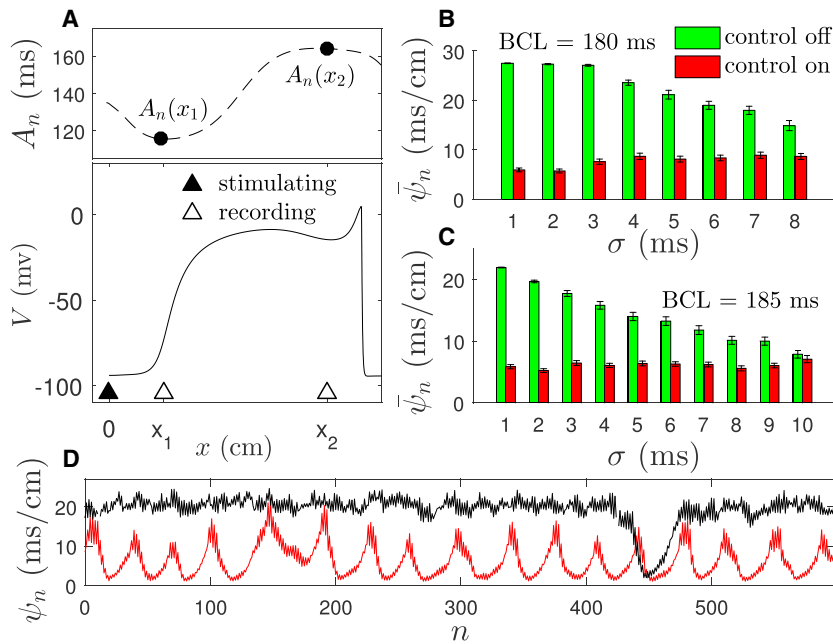
FIGURE 10 (*A*) The upper and lower plots describe the placement of stimulating and recording electrodes to implement the control strategy (Eq. 17). Although the complete dashed APD profile is not measured, a large enough difference between the recorded APD at two sites implies that discordant alternans has developed, triggering the controller to activate. (*D*) Profiles of ψ_n for BCL = 185 ms and $\sigma = 2$ ms both with (*red lines*) and without (*black lines*) the control strategy (Eq. 17) applied. (*B* and *C*) Average values of ψ_n over the course of simulations with and without active control over various values of σ and BCL. To see this figure in color, go online.

dispersion of APDs when the system is uncontrolled (*green bars*) and when the control strategy (Eq. 17) is applied (*red bars*) for different values of BCL and σ. As in the previous sections, each set of parameters is simulated for more than 4000 beats. The SE of the mean is represented by bars and is calculated assuming statistical independence after 30 beats; measurements are taken at this interval to calculate the mean $\pm$ SE. When the control is applied, $\overline{\psi}_n$ grows slightly as variability increases, but it is always lower when compared to the uncontrolled system.

Stochastic pacing and discordant alternans caused by calcium instabilities

The behavior when alternans is driven by calcium instabilities can differ significantly from the case where alternans is driven by steep APD restitution. Because calcium diffusion occurs on a much slower timescale, calcium dynamics can vary significantly over short distances (41), and in some cases, discordant alternans in calcium cycling can occur within individual cells (86). Even though calcium dynamics are not directly coupled between cells, indirect coupling due to voltage differences does exist. These factors lead to a more complicated relationship between calcium and voltage nodal dynamics during discordant alternans. Previous studies (41,87) have investigated the behavior of alternans solutions on a 1-D medium when individual cellular dynamics are close to the period-doubling bifurcation, so that alternans can be understood from the point of view of a continuous partial differential equation. Such assumptions do not hold when pacing is variable, because the variability can cause large jumps in the APDs on a beat-to-beat basis. Here, we briefly investigate the effect of stochastic pacing

when alternans is driven by instabilities in calcium dynamics in simulations of Eq. 2 using the Shiferaw-Fox model (61) to simulate the cellular ionic dynamics. Model parameters are identical to those used for the 1-D simulations presented in Fig. 2.

We define $C_n(x)$ as the peak value of the intracellular calcium concentration of the nth beat and the node location, w_n^*, defined such that $C_n(w_n^*) - C_{n-1}(w_n^*) = 0$. The location of the APD node is defined as x_n^*, as in previous sections. Fig. 11, *A* and *B*, shows the coupled behavior of the calcium and voltage dynamics in the presence of stochastic pacing. The two nodes tend to move together, with the location of the calcium node reacting slowly to changes in the voltage node. Furthermore, the calcium node tends to stay slightly closer than the APD node to the paced end of the tissue. Variance in the location of the nodes also increases as σ increases, much as in the previous examples. For large enough excursions toward the paced end, the node is absorbed temporarily, resulting in concordant alternans. Much as in previous examples, premature beats tend to drive each node toward (away from) the paced node when the slope of the current APD profile is positive (negative), allowing for the implementation of the control strategy (Eq. 17). In this example with calcium alternans, we take $A_T = 15$ ms and $\omega = 20$ ms, with $x_1 = 2$ cm and $x_2 = 8$ cm. Fig. 11 *C* gives a representative plot of ψ_n from Eq. 4 for two simulations with (*red line*) and without (*black line*) the control strategy applied. Fig. 11, *D* and *E*, shows the mean value of ψ_n plotted for various values of γ and σ with BCL = 310 ms, with and without control. In simulations where σ is low and the control is applied, the resulting value is similar to that in simulations where σ is large and no control is applied.
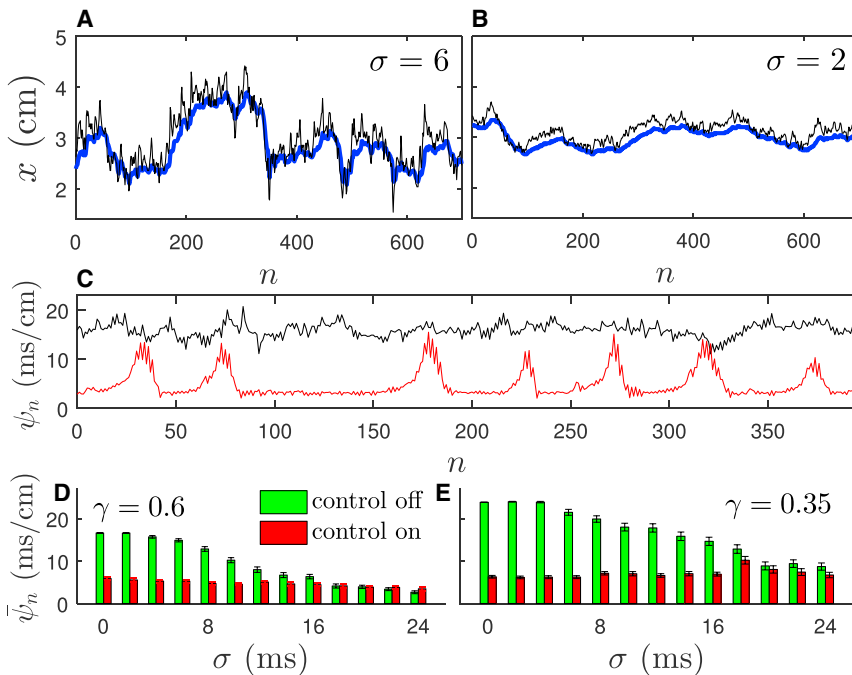
FIGURE 11 (*A* and *B*) Relationship between the calcium node (*thick blue line*) and the APD node (*thin black line*) for different values of σ. (*C*) Representative snapshot of the maximal dispersion in APDs with and without control (*red* and *black* lines, respectively) for $\sigma = 6$. (*D* and *E*) Mean values of ψ_n for $\gamma = 0.6$ (*D*) and 0.35 (*E*) and various values of σ, with and without the control strategy applied. Mean $\pm$ SE bars are calculated in the same fashion as in Fig. 2. To see this figure in color, go online.

Due to the coupling between voltage and calcium dynamics, in this example, we do not have an explicit formula for the nodal dynamics during discordant alternans caused by calcium instabilities. The intuition for the control strategy (Eq. 17) as applied to the cardiac system with calcium alternans comes from studying the dynamics when alternans is caused by steep APD restitution. However, unlike in the previous sections, we do not have explicit estimates for how strong the applied control should be to drive the node to the boundary. Nevertheless, Eq. 17 still provides an effective control strategy.

Stochastic pacing in 2-D models

In the previous sections, the effect of stochastic pacing on the persistence of discordant alternans was investigated in 1-D models of cardiac tissue. On 2-D surfaces, paced tissue can still form discordant alternans, with nodal lines separating regions in space where the alternans is out of phase (45–47,79). Authors of previous work have observed nodal lines that travel toward the pacing location when the BCL decreases (46,47). Here, we investigate the effect of stochastic pacing in 2-D simulations of Eq. 2.

Initially, we consider $\delta_n = \sigma\eta_n$, where η_n represents a zero-mean, unit-variance Gaussian random variable, and $\sigma > 0$. Taking BCL = 189 ms and $\sigma > 3$, the dynamical behavior is qualitatively similar to that in the 1-D simulations, with alternans transitioning between discordant and concordant, as shown in Fig. 12, *A* and *B*, respectively. During discordant alternans, nodal lines are formed by the intersection between planes representing the APD on two

successive beats, i.e., locations in space for which successive APDs are identical. Without stochastic pacing, a stable, stationary nodal line forms at steady state. For simulations of $\sigma = 1$, Fig. 12 *C* shows multiple nodal lines plotted every 15 beats over the course of a single simulation. The stochastic behavior of these nodal lines is similar to that in 1-D simulations, with a significant concentration found at a radius of ~ 5.5 cm. Furthermore, for larger values of σ, these lines take larger excursions from their mean values, occasionally disappearing through the paced end and re-forming in the far corner. In Fig. 12 *D*, the maximal value of σ is $\sim 4\%$ of the nominal BCL.

Quantitative analysis becomes more difficult in 2-D, requiring explicit knowledge of the shape of the nodal lines to predict their beat-to-beat dynamics (79). Qualitatively, however, the behavior is similar to that in the 1-D system where stable nodal lines form at points where the effects of CV restitution and electrotonic coupling are balanced, and premature pulses push the nodal lines toward or away from the pacing site, depending on the sign of the gradient of the APD profile. With the intuition developed using the control strategy (Eq. 17) from the previous section in 1-D tissue, we investigate an analogous discordant alternans elimination strategy on the 2-D domain:

$$\delta_n = \min\left(\sigma\eta_n, \delta_n^c\right),$$
$$\delta_n^c = \begin{cases} -\omega, & \text{if } A_n(x_1, y_1) - A_n(x_2, y_2) < -A_T, \\ \infty, & \text{otherwise.} \end{cases} \quad (18)$$

Similar to Eq. 17, the formulation of this control strategy assumes that some variability in the pacing rate already exists in the system and that we can give a beat prematurely but
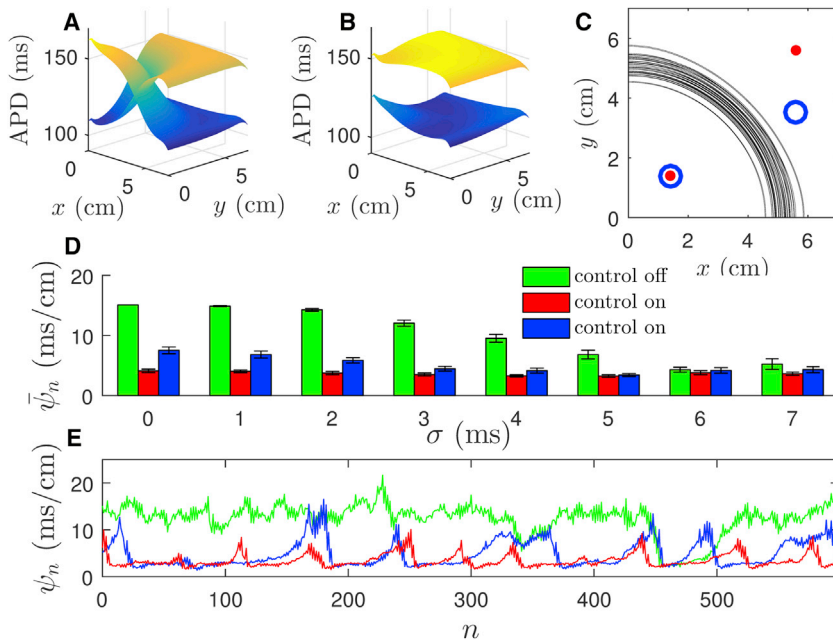
FIGURE 12 (*A* and *B*) Examples of discordant and concordant alternans, respectively, in 2-D simulations. (*C*) Snapshots of nodal lines taken every 15 beats in simulations with $\sigma = 1$ ms. Red dots and blue circles show the placement of two different APD recording locations used in these simulations; red and blue bars and traces from (*D*) and (*E*) correspond to results obtained with the recording locations of the same color from (*C*). (*D*) Average maximal local dispersion of APDs, $\overline{\psi}_n$, with and without using the control strategy (Eq. 18), for various values of σ. (*E*) Representative plots of ψ_n over the course of simulations with $\sigma = 3$ ms, with (*red* and *blue traces*) and without (*green trace*) control. To see this figure in color, go online.

cannot delay a beat that occurs naturally. Practically, we require (x_1, y_1) to be closer to the pacing site than (x_2, y_2) and spaced far enough apart so that nodal lines form between these recording electrodes. Note the similarity between the 2-D control strategy (Eq. 18) and the 1-D version (Eq. 17). We apply the control strategy (Eq. 18) using $\omega = 10$ ms, $A_T = 20$ ms, and two different placements of the recording electrodes. In the first set of simulations, $(x_1, y_1) = (1.4 \text{ cm}, 1.4 \text{ cm})$ and $(x_2, y_2) = (5.6 \text{ cm}, 5.6 \text{ cm})$, with node locations in Fig. 12 *C* represented by red dots. In the second set of simulations, $(x_1, y_1) = (1.4 \text{ cm}, 1.4 \text{ cm})$ and $(x_2, y_2) = (5.6 \text{ cm}, 3.5 \text{ cm})$, with locations in Fig. 12 *C* represented by blue circles.

As was the case for 1-D simulations, there is an inverse relationship between σ and $\overline{\psi}_n$ when no control is applied (Fig. 12 *D*, *green bars*). Each data point is determined from a simulation of >1000 beats after allowing sufficient time for transient behavior to die out; the mean ± SE values are calculated assuming statistical independence of measurements after 30 beats. In each of these simulations, conduction block occurs less than once in every 400 beats at the pacing site. The control strategy (Eq. 18) is able to reduce $\overline{\psi}_n$ for both placements of the recording electrodes. However, for the sites represented by red dots in Fig. 12 *C*, the control is more effective at reducing discordant alternans than the electrode placement represented by blue circles. This is particularly true for small values of σ. Because nodal lines tend to form opposite the pacing cite and migrate toward the paced end, the red electrode placement is able to detect discordant alternans sooner than the blue electrode placement, activating the premature pulses sooner to eliminate discordant alternans. For the red electrode placement, the efficacy of the control strategy does not depend strongly on σ.

For the blue electrode placement, higher values of σ cause greater variance in the location of the nodal lines, hastening the detection of discordant alternans and its subsequent elimination.

Fig. 12 *E* shows representative plots of ψ_n with $\sigma = 3$ ms with (*red* and *blue traces*) and without control (Eq. 18) (*green trace*). In the controlled case, nodal lines are quickly driven toward and absorbed by the paced corner of the tissue, restoring concordant alternans. Although discordant alternans eventually reforms, it never lasts for more than a few beats once the control is engaged. Compared with the system behavior when control is off, alternans is almost exclusively discordant when $\sigma < 3$. As mentioned previously, a less effective electrode placement (*blue trace*) can delay the detection of discordant alternans, allowing ψ_n to grow to larger values compared to the more effective electrode placement (*red trace*).

DISCUSSION

Although depressed HRV is positively correlated with a patient's susceptibility to sudden cardiac death (3,4,6), it is not known whether there is a causal link between low HRV and cardiac fibrillation; the results of this numerical study suggest the possibility of such a mechanistic link. In simulations where the pacing rate is taken from a Gaussian distribution, when the variance is low, sustained discordant alternans is able to form in paced cardiac tissue, an arrhythmia that has been implicated in the formation of reentrant cardiac arrhythmias (34,35). As the variance of stochastic pacing increases, concordant alternans becomes more prevalent. This general behavior was observed in simulations regardless of whether cellular alternans was driven

by steep APD restitution or instabilities in the intracellular calcium dynamics, and it was seen on 1-D and 2-D domains.

This behavior is somewhat counterintuitive considering that stochastic pacing can cause alternans to develop in single cells even when the underlying deterministic system has stable period-1 behavior, as previously investigated in (58) and (59). By analyzing a map of the calcium and APD restitution dynamics, we show that even small a variance in the BCL can lead to a large variance in APD when the deterministic system has dynamics that are close to the period-doubling bifurcation. This amplification allows alternans to form even when the variance in the pacing rate is small. Although stochastic pacing can facilitate the formation of cellular alternans and allows for more severe alternans on a beat-to-beat basis, it does not lead to worsening spatial dispersion of APD alternans in 1-D and 2-D simulations. We surmise that although beat-to-beat variability of alternans may increase due to stochastic pacing, a premature (delayed) beat will excite all cells sooner (later) than expected, increasing (decreasing) the APDs throughout the entire domain but doing little to influence the spatial dispersion.

To simplify the analysis of the formation and maintenance of discordant alternans in tissue in 1-D models, we focus on the dynamic behavior of the APD nodes. Although the nodal dynamics depend on multiple nonlinear factors, including electrotonic and CV restitution effects (cf. Eq. 12), we find that the variance in the node location can be well approximated starting with a simplified Eq. 14, which is derived by assuming a linear relationship between the node location and cycle length and a constant relation between the node location and electrotonic effects on the APD restitution. For relatively small variance in the pacing rate, we show that the variance of the node location should scale proportionally and verify this behavior in numerical simulations. As the variance increases, the node has a tendency to be absorbed through the paced end of the tissue, causing the alternans to temporarily revert to a concordant state. The mechanism by which stochastic pacing imparts protection against discordant alternans could be interpreted as a mean-first-passage-time problem (78) from a potential well, as illustrated in Fig. 9. As variability increases, mean escape time decreases until the discordant alternans state is destroyed almost as soon as it can form. Quantitative analysis is much more difficult in 2-D models. Nevertheless, numerical simulations show that nodal lines in 2-D models move in a manner qualitatively similar to that of nodes that form in 1-D simulations. These nodal lines are occasionally absorbed through the paced end of the tissue, temporarily restoring concordant alternans. It would be of interest to investigate whether similar behavior could be observed on domains that take into account the complicated 3-D geometry of living hearts.

Our results indicate that the primary mechanism by which stochastic pacing decreases the tendency for a system to display discordant alternans is through driving nodes to be absorbed through the paced end of the boundary. Therefore, we would only expect this to inhibit the formation of discordant alternans when the tissue has the propensity to form discordant alternans with a single APD node; otherwise, variability will only change the number of nodes present at a given time, but will not eliminate discordant alternans entirely. Although numerical models have been shown to display discordant alternans with several nodes on particularly long domains (35,40,88), experimental preparations commonly observe the stable formation of single nodal lines between the pacing site and the tissue boundary at moderate levels of pacing, with more complicated patterns emerging as the tissue is paced at cycle lengths closer to the refractory limit (44–48). In this study, we have not investigated the effect of stochastic pacing on discordant alternans that forms due to other factors, for example, premature beats (35,42); however, preliminary simulations (data not shown) suggest that stochastic pacing can help restore concordant alternans in the aforementioned scenario, even when nodes have a tendency to become pinned in place (41). Furthermore, bistability between alternans and 2:1 behavior (i.e., one action potential for every two stimuli) has been observed in experimental preparations (89) and it would be of interest to investigate the effect this behavior plays on the formation of discordant alternans and whether it could be exploited in future control strategies.

Analysis of nodal dynamics during discordant alternans yields a relatively simple control strategy by which appropriately timed premature beats can be applied to inhibit the formation of discordant alternans. Although it would be better to develop a control strategy to eliminate both concordant and discordant alternans from the system, such control strategies generally require either small domains with relatively small-amplitude alternans or multiple stimulating electrodes placed throughout the tissue to be effective (82–84), as full spatial control of alternans with single-site stimulation typically fails for domains that are too large (85). The control strategy employed in this study suggests that it may be feasible to convert discordant alternans to concordant alternans using single-site stimulation on relatively large domains. We emphasize that these are preliminary numerical results obtained on heterogeneous domains that do not take into account the complicated geometry of the heart. The thresholds for determining when to give a premature pulse, as suggested by (75) and (82), may be too simple to detect discordant alternans in real hearts, as the APD has been observed to vary spatially even when alternans is not present (45). Additionally, further testing would be required to ensure that the application of such premature beats would not induce fibrillation. It would be worthwhile to investigate possible strategies that can eliminate discordant alternans by stabilizing the concordant alternans state. This control objective might be more feasible from a controllability perspective than the goal of eliminating alternans entirely and would still serve to eliminate the spatial

dispersion of refractoriness, which has been implicated as a precursor to more serious reentrant arrhythmias.

This study is certainly not without limitations. Foremost, in this work, we have only considered relatively simple domains on which discordant alternans forms. Experimental results (45–48) suggest that the complicated three-dimensional geometry of intact hearts may play a role in the formation of more spatially complicated alternans patterns that are not considered here. Furthermore, we have not considered the effect of spatial heterogeneity in the cardiac substrate, which can exacerbate the severity of discordant alternans (43). Analytically, we have considered the dynamical behavior of nodes that form during discordant alternans, but we have not explicitly analyzed the effect of HRV formation or discordant alternans starting from concordant alternans. Further investigation could be useful, particularly if a control strategy could be found that completely stops discordant alternans from forming. Throughout this work, we have incorporated HRV by adding a normally distributed random variable to the nominal BCL and have neglected the power spectrum of HRV in living patients (Eq. 4). It would be of interest to investigate the effect of the specific components of HRV on the formation of discordant alternans modulating their relative amplitudes to observe the effect on the formation of alternans. Additionally, the metric (Eq. 4) that defines the severity of dispersion caused by discordant alternans would be difficult to apply to real tissue and may not be able to distinguish between concordant and discordant alternans when APD dispersion is significantly affected by both heterogeneity (66) and differences in electrotonic currents throughout the tissue (67–69). These limitations would need to be addressed in experiments on real tissue.

The results of these computational simulations suggest a potential mechanism by which HRV could decrease the tendency toward formation of discordant alternans, thereby making fibrillation less likely. However, we have not explicitly tested this hypothesis. Although the average severity dispersion caused by discordant alternans was found to decrease significantly as the variance of stochastic pacing increases, occasional spikes in alternans severity occur during simulations, along with occasional conduction block as variability becomes more severe. Such factors may have the opposite effect of promoting fibrillation. It would be of great interest to investigate the relation between HRV and the ability to induce ventricular fibrillation with in vivo experimental preparations to definitively test this hypothesis.

APPENDIX A: ANALYSIS OF STOCHASTIC PACING AND ALTERNANS IN SINGLE CARDIOMYOCYTES

In Methods, Eq. 5 represents a simplification of the interplay in the calcium and voltage dynamics of single-cell simulations (Eq. 1) and can be rewritten as

$$
\begin{aligned}
A_{n+1} &= f(\text{BCL} + \sigma\eta_n - A_n) + \xi(\rho(\text{BCL} + \sigma\eta_n - A_n) \\
&\quad -g(C_n)), \\
C_{n+1} &= \rho(\text{BCL} + \sigma\eta_n - A_n) - g(C_n),
\end{aligned}
\tag{A1}
$$

where the terms have been rearranged so that the values on the $(n+1)$th beat can be obtained directly from values on the nth beat. Suppose that the mapping (Eq. A1) admits a stable, period-1, alternans-free solution in the absence of cycle length variability, i.e., for a given BCL, $A^* = f(\text{BCL} - A^*) + \xi(\rho(\text{BCL} - A^*) - g(C^*))$, $C^* = \rho(\text{BCL} - A^*) - g(C^*)$, and $D^* = \text{BCL} - A^*$. Linearizing Eq. A1 around this fixed point yields

$$
x_{n+1} = Px_n + Q\sigma\eta_n,
\tag{A2}
$$

where

$$
P = \begin{bmatrix} -f' - \xi' g' & -\xi' g' \\ -\rho' & -g' \end{bmatrix}, \quad Q = \begin{bmatrix} f' + \xi' g' \\ \rho' \end{bmatrix},
$$

$$
x_n = \begin{bmatrix} A_n - A^* \\ C_n - C^* \end{bmatrix}
$$

and $f' \equiv \frac{\partial f}{\partial D_n}\big|_{D^*}$, $\rho' \equiv \frac{\partial \rho}{\partial D_n}\big|_{D^*}$, $g' \equiv \frac{\partial g}{\partial C_n}\big|_{C^*}$, and $\xi' \equiv \frac{\partial \xi}{\partial C_n}\big|_{C^*}$. To understand the long-term dynamics of the mapping, Eq. A2 can be written in terms of its initial conditions:

$$
\begin{aligned}
x_1 &= Px_0 + Q\sigma\eta_1 \\
x_2 &= P^2 x_0 + PQ\sigma\eta_1 + Q\sigma\eta_2 \\
x_3 &= P^3 x_0 + P^2 Q\sigma\eta_1 + PQ\sigma\eta_2 + Q\sigma\eta_3 \\
&\vdots \\
x_n &= P^n x_0 + \sigma\sum_{k=0}^{n-1} P^k Q\eta_{n-k}.
\end{aligned}
\tag{A3}
$$

Substituting Eq. A3 into Eq. A2 yields the relation

$$
x_{n+1} - x_n = (P - I)P^n x_0 + \sigma(P - I)\sum_{k=0}^{n-1} P^k Q\eta_{n-k}
$$
$$
+ Q\sigma\eta_{n+1},
\tag{A4}
$$

where I is an appropriately sized identity matrix. Because Eq. A4 is the sum of a linear combination of normally distributed and independent random variables, $x_{n+1} - x_n$ will also follow a normal distribution. Particularly, the mean and variance of $A_{n+1} - A_n$ are

$$
\begin{aligned}
\mu(n, x_0) &= \text{mean}(A_{n+1} - A_n) \\
&= E\left[e_1^{\mathrm{T}}(P - I)P^n x_0 + \sigma e_1^{\mathrm{T}}(P - I)\sum_{k=0}^{n-1} P^k Q\eta_{n-k} + e_1^{\mathrm{T}} Q\sigma\eta_{n+1}\right], \\
&= e_1^{\mathrm{T}}(P - I)P^n x_0, \\
\nu(n) &= \text{var}(A_{n+1} - A_n) \\
&= E\left[(A_{n+1} - A_n - \text{mean}(A_{n+1} - A_n))^2\right], \\
&= \sigma^2\left[e_1^{\mathrm{T}}(P - I)\sum_{k=0}^{n-1}\left[P^k QQ^{\mathrm{T}}(P^k)^{\mathrm{T}}\right](P - I)^{\mathrm{T}} e_1 + e_1^{\mathrm{T}} QQ^{\mathrm{T}} e_1\right],
\end{aligned}
\tag{A5}
$$

where $e_1 = [0\ 1]^T$, E denotes the expected value, and superscript T indicates the matrix transpose. The second line of Eq. A5 is obtained using $E[\eta_i] = 0$, and the third line is obtained using $E[\eta_i\eta_i] = 1$, and $E[\eta_i\eta_j] = 0$ for $i \neq j$. For a stable alternans-free solution, the $\lim_{n\to\infty}(P^n)$ approaches the zero matrix so that μ also approaches zero and is invariant to initial conditions. We can also consider the variance as n approaches infinity. Suppose the matrix R exists such that,

$$\lim_{n\to\infty}\left(\sum_{k=0}^{n-1}\left[P^k QQ^T\left(P^k\right)^T\right]\right) = R. \tag{A6}$$

Manipulation of Eq. A6 yields

$$P\lim_{n\to\infty}\left(\sum_{k=0}^{n-1}\left[P^k QQ^T\left(P^k\right)^T\right]\right)P^T = PRP^T,$$

$$\left(P\lim_{n\to\infty}\left(\sum_{k=1}^{n-1}\left[P^k QQ^T\left(P^k\right)^T\right]\right)P^T + QQ^T\right) \tag{A7}$$
$$-QQ^T = PRP^T,$$

$$PRP^T - R + QQ^T = 0,$$

so that R is the solution to the discrete-time Lyapunov equation (90) and is guaranteed to exist when P is stable. Substituting Eq. A6 into Eq. A5 yields the relation

$$\nu_\infty \equiv \lim_{n\to\infty} \nu(n) = \sigma^2 e_1^T\left[(P-I)R(P-I)^T + QQ^T\right]e_1. \tag{A8}$$

APPENDIX B: NODAL DYNAMICS WITH STOCHASTIC PACING WHEN DISCORDANT ALTERNANS IS DRIVEN BY VOLTAGE INSTABILITIES

Here, we derive the relationship described by Eq. 12, which can be used to understand the dynamical behavior of discordant alternans nodal dynamics on 1-D domains.

To begin, suppose that for a system (Eq. 2) that exhibits discordant alternans, there exists a node at x^*_{n+2} for which $A_{n+1}(x^*_{n+2}) = A_{n+2}(x^*_{n+2})$. Expanding each of these terms near the fixed point allows us to write

$$A_{n+2}(x) - A_{n+1}(x) = \left(\frac{\partial A_{n+2}}{\partial x} - \frac{\partial A_{n+1}}{\partial x}\right)\Delta x + \mathcal{O}(\Delta x^2), \tag{B1}$$

where $\Delta x = x - x^*_{n+2}$ and the partial derivatives are evaluated at x^*_{n+2}. For convenience of notation, we will let $\phi_{n+2} \equiv (\partial A_{n+2}/\partial x - \partial A_{n+1}/\partial x)$ evaluated at x^*_{n+2}. Substituting Eq. 9 for $A_{n+2}(x)$ and $A_{n+1}(x)$ into the left hand side of Eq. B1 and rearranging yields

$$f(D_{n+1}(x)) = f(D_n(x)) + \alpha_n(x) - \alpha_{n+1}(x) + \phi_{n+2}\Delta x,$$
$$\approx f\left(D_n(x) + \frac{\alpha_n(x) - \alpha_{n+1}(x) + \phi_{n+2}\Delta x}{f'|_{D_n(x)}}\right), \tag{B2}$$

where $f' \equiv \partial f/\partial D_n$. Equation B2 is valid to leading order $(\alpha_n(x) - \alpha_{n+1}(x) + \phi_{n+2})/f'|_{D_n(x)}$. Because f is typically a strictly monotonically increasing function of the DI, equality in Eq. B2 implies

$$D_{n+1}(x) = D_n(x) + \frac{\alpha_n(x) - \alpha_{n+1}(x) + \phi_{n+2}\Delta x}{f'|_{D_n(x)}}. \tag{B3}$$

Now, using Eq. 10 we can write $D_{n+2}(x) - D_{n+1}(x) = T_{n+2}(x) - A_{n+2}(x) - T_{n+1}(x) + A_{n+1}(x)$. Substituting Eqs. B3, B1, and 11 into this expression and rearranging yields the relation

$$D_{n+2}(x) - D_n(x) = \delta_{n+2} - \delta_{n+1} + \left(\frac{1}{f'|_{D_n(x)}} - 1\right)\phi_{n+2}\Delta x$$
$$+ \frac{\alpha_n(x) - \alpha_{n+1}(x)}{f'|_{D_n(x)}}$$
$$+ \underbrace{\int_0^x\left[\frac{1}{c(D_{n+2}(x'))} - \frac{2}{c(D_{n+1}(x'))} + \frac{1}{c(D_n(x'))}\right]dx'}_{\Lambda_{n+2}(x)}. \tag{B4}$$

The term $\Lambda_n(x)$ is defined in the above equation for convenience of notation and captures the effect of CV restitution. The relationship described by Eq. B4 represents an explicit integral equation for the next DI and allows us to calculate the values of $A_{n+3}(x)$ in the vicinity of x^*_{n+2} as follows:

$$A_{n+3}(x) = f(D_n(x) + (D_{n+2}(x) - D_n(x))) + \alpha_{n+2}(x),$$
$$= f(D_n) + f'|_{D_n(x)}(D_{n+2}(x) - D_n(x)) + \alpha_{n+2}(x),$$
$$= A_{n+1}(x) - \alpha_n(x) + f'|_{D_n(x)}(D_{n+2}(x) - D_n(x)) + \alpha_{n+2}(x). \tag{B5}$$

Here, the last line is obtained using Eq. 9. Subtracting A_{n+2} from both sides yields

$$A_{n+3}(x) - A_{n+2}(x) = A_{n+1}(x) - A_{n+2}(x) + f'|_{D_n(x)}(D_{n+2}(x) - D_n(x)) + \alpha_{n+2}(x) - \alpha_n(x),$$
$$= -\phi_{n+2}\Delta x + f'|_{D_n(x)}(D_{n+2}(x) - D_n(x)) + \alpha_{n+2}(x) - \alpha_n(x), \tag{B6}$$

where the last line is obtained using the relation described by Eq. B1. Finally, setting the left hand side of Eq. B6 equal to zero, substituting Eq. B4 and rearranging yields the relation

$$x^*_{n+3} - x^*_{n+2} = \frac{1}{\phi_{n+2}}\left[\delta_{n+2} - \delta_{n+1}\right.$$
$$\left. + \frac{\alpha_{n+2}(x^*_{n+3}) - \alpha_{n+1}(x^*_{n+3})}{f'|_{D_n(x^*_{n+3})}} + \Lambda_{n+2}(x^*_{n+3})\right]. \tag{B7}$$

Equation B7 is a complicated, implicit equation describing the nodal movement as a function of the previous two perturbations to the nominal cycle length. In the sections to follow, we will investigate the effect of approximations that simplify Eq. B7 to further manipulate and understand the perturbed dynamics.

APPENDIX C: NODAL DYNAMICS WITH GAUSSIAN HEART RATE VARIABILITY

Here, we derive the relationship described by Eq. 16, describing how the variance in the node location varies as a function of the variance HR. Beginning with the relation in Eq. B7, and substituting the simplified relations from Eqs. 14 and 15 into Eq. B7 yields

$$x_{n+3}^* - x_{n+2}^* = \frac{1}{\phi_{n+2}}\left[\delta_{n+2} - \delta_{n+1} + (-1)^n\left(J + a + kx_{n+3}^*\right)\right].$$

(C1)

Next, we make the assumption that HRV is modeled as a series of normally distributed random perturbations. As was the case in the zero-dimensional analysis, we take $\delta_n = \sigma\eta_n$, where η_n is an independent random variable drawn from a Gaussian distribution with mean zero and unit variance, with σ representing the magnitude of the variability. Substituting this relation along with Eq. 13 yields

$$x_{n+3}^* - x_{n+2}^* = \frac{1}{\beta}\left[\sigma(\eta_{n+2} - \eta_{n+1})(-1)^n + J + a + kx_{n+3}^*\right],$$

(C2)

which can be simplified by letting $y_n \equiv x_n^* + (J + a)/k$ and reindexing to

$$y_{n+1} - y_n = \frac{1}{\beta}\left[\sigma(\eta_n - \eta_{n-1})(-1)^n + ky_{n+1}\right],$$

$$\left(1 - \frac{k}{\beta}\right)y_{n+1} = y_n + \frac{(-1)^n}{\beta}(\sigma(\eta_n - \eta_{n-1})), \quad \text{(C3)}$$

$$y_{n+1} = \lambda y_n + \frac{(-1)^n}{\beta - k}(\sigma(\eta_n - \eta_{n-1})),$$

where $\lambda = 1/(1 - (k/\beta))$. Equation C3 implies that in the absence of variability (when $\sigma = 0$), the node location should settle to a stable fixed point at $x_{fp} = -(J + a)/k$ provided that $|\lambda| < 1$ and $x_{fp} \in [0, L]$, where L is the length of the tissue. We assume that the unperturbed system has a stable discordant alternans solution with a single node, so $|\lambda| < 1$. In this case, composing the map from Eq. C3 with itself, we can write Eq. C3 as an explicit function of an initial measurement, y_0:

$$y_n = \lambda^n y_0 + \frac{\sigma(\lambda + 1)}{\beta - k}\sum_{k=0}^{n-2}\left[(-1)^{n-1-k}\lambda^k \eta_{n-1-k}\right]$$

$$- \frac{\sigma\lambda^{n-1}}{\beta - k}\eta_0 + \frac{\sigma(-1)^n}{\beta - k}\eta_n.$$

(C4)

Because y_n is the sum of a series of Gaussian random variables, y_n is also a random variable with mean and variance ($\mu(n, y_0)$ and $\nu(n)$, respectively),

$$\mu(n, y_0) = \lambda^n y_0,$$

$$\nu(n) = \frac{\sigma^2(\lambda + 1)^2}{(\beta - k)^2}\sum_{k=0}^{n-2}\lambda^{2k} + \frac{\sigma^2(\lambda^{2(n-1)} + 1)}{(\beta - k)^2}. \quad \text{(C5)}$$

In the limit as n approaches infinity, the mean approaches zero, and the variance approaches

$$\lim_{n \to \infty}\nu(n) \equiv \nu_\infty = \frac{\sigma^2}{(\beta - k)^2}\left[\frac{(\lambda + 1)^2}{(1 - \lambda^2)} + 1\right]$$

$$= \frac{\sigma^2}{(\beta - k)^2}\left[\frac{-2(\beta - k)}{k}\right] \quad \text{(C6)}$$

$$= \frac{-2\sigma^2}{k\beta - k^2}.$$

Note here that $k\beta < 0$; otherwise, either $|\lambda| > 1$ or $-1 \le \lambda < 0$; the former implies that the fixed point is unstable, and the latter would require unrealistically large CV restitution. The above equation states that given enough time to forget initial conditions, the variance of the node location is proportional to the square of the variability in HR timing and inversely related to the magnitudes of both β and k.

APPENDIX D: DERIVATION OF A CONTROL STRATEGY FOR MANIPULATING DISCORDANT ALTERNANS

Consider the simplified Eq. C1 where $(J + a + kx_{fp}) = 0$ for some x_{fp} in the domain so that stable discordant alternans forms. To drive the node toward the paced end of the tissue, by inspection we can require

$$\text{sign}(\phi_{n+2})[\delta_{n+2} - \delta_{n+1}] < -\left|kx_{fp}^*\right|. \quad \text{(D1)}$$

The above relation ensures that the righthand side of Eq. C1 is less than zero so that the node will always be moving to the left, where it will eventually be absorbed by the boundary. We assume that with HRV, δ_n can be taken to be a normally distributed random variable, $\sigma\eta_n$, as defined in the previous section. Assuming that we have the ability to give a premature stimulus but cannot delay the timing of a pulse, we can modulate the pulse timing so that

$$\delta_{n+2} = \min(\sigma\eta_{n+2}, \delta_{n+2}^c), \quad \text{(D2)}$$

where Δ_{n+2}^c is a control target. With the requirement of Eq. D1 in mind, and recalling that the sign of ϕ_n alternates on a beat-to-beat basis, consider the pacing strategy

$$\delta_{n+2}^c = \begin{cases} -\omega, & \text{for } \phi_{n+2} > 0, \\ \infty, & \text{for } \phi_{n+2} \le 0, \end{cases} \quad \text{(D3)}$$

where $\omega > \left|kx_{fp}\right|$. Recall from the definition of δ_n from Eq. 11, when δ_n^c is negative, the cycle length is smaller than its nominal value (incorporated, e.g., by applying premature pulse). Supposing that $\phi_{n+2} > 0$, then $\phi_{n+1} < 0$ and $E[\delta_{n+1}] = 0$, because the control strategy will not elicit a premature pulse. The random variable δ_{n+2} can only take values below $-\omega$ so that $E[\delta_{n+2}] < -\omega$. Therefore, using the pacing protocol from Eq. D3, $E[\text{sign}(\phi_{n+2})(\delta_{n+2} - \delta_{n+1})] < -\omega < -kx_{fp}^*$, so that on average Eq. D1 is satisfied, influencing the node to move toward the paced end of the tissue. In practice, the linear relationship between Λ_n and x_0^* begins to flatten near $x = 0$ so that $\omega \approx \left|kx_{fp}\right|$ provides an order-of-magnitude estimate for the required size of ω.

The control strategy of Eq. D3 does not require active control when alternans is concordant, and requires some feedback about the state of the system. If the tissue is only long enough for a single node to form, one can place two recording electrodes at either end of the tissue at $x = x_1$ and $x = x_2$ to practically implement (D3)

$$\delta_{n+2}^{c} = \begin{cases} -\omega, & \text{if } A_{n+2}(x_1) - A_{n+2}(x_2) < -A_{\text{T}}, \\ \infty, & \text{otherwise.} \end{cases} \quad \text{(D4)}$$

Here $A_{\text{T}} > 0$ is some threshold used to trigger the control, and $0 \leq x_1 < x_2$. Fig. 10 A, upper and lower, describes the setup of the control strategy described in Eq. 17, where two recording electrodes monitor action potentials to decide whether to elicit a premature stimulus. Depending on the system, action potentials may not be finished by the time the controller must decide whether to give a premature stimulus or not. In this case, one could instead replace the first condition of Eq. D4 by

$$\delta_{n+2}^{c} = -\omega, \text{ if } A_{n+1}(x_2) - A_{n+1}(x_1) < -A_{\text{T}}.$$

Here, we assume $A_{n+1}(x_2) - A_{n+1}(x_1) \approx A_{n+2}(x_1) - A_{n+2}(x_2)$, with the alternans profiles being close to mirror images of each other.

AUTHOR CONTRIBUTIONS

D.W. designed the research. D.W. performed the research and analyzed the data. D.W. and B.E. wrote the article.

ACKNOWLEDGMENTS

REFERENCES

1. Rajendra Acharya, U., K. Paul Joseph, …, J. S. Suri. 2006. Heart rate variability: a review. *Med. Biol. Eng. Comput.* 44:1031–1051.

2. Bilchick, K. C., B. Fetics, …, R. D. Berger. 2002. Prognostic value of heart rate variability in chronic congestive heart failure (Veterans Affairs' Survival Trial of Antiarrhythmic Therapy in Congestive Heart Failure). *Am. J. Cardiol.* 90:24–28.

3. Kleiger, R. E., J. P. Miller, …, A. J. Moss. 1987. Decreased heart rate variability and its association with increased mortality after acute myocardial infarction. *Am. J. Cardiol.* 59:256–262.

4. Task Force of the European Society of Cardiology and the North American Society of Pacing and Electrophysiology. 1996. Heart rate variability. Standards of measurement, physiological interpretation, and clinical use. *Eur. Heart J.* 17:354–381.

5. La Rovere, M. T., G. D. Pinna, …, F. Cobelli. 2003. Short-term heart rate variability strongly predicts sudden cardiac death in chronic heart failure patients. *Circulation.* 107:565–570.

6. Xhyheri, B., O. Manfrini, …, R. Bugiardini. 2012. Heart rate variability today. *Prog. Cardiovasc. Dis.* 55:321–331.

7. Bigger, J. T., Jr., J. L. Fleiss, …, J. N. Rottman. 1992. Frequency domain measures of heart period variability and mortality after myocardial infarction. *Circulation.* 85:164–171.

8. Acharya U., R., N. Kannathal, and S. M. Krishnan. 2004. Comprehensive analysis of cardiac health using heart rate signals. *Physiol. Meas.* 25:1139–1151.

9. Huikuri, H. V., T. H. Mäkikallio, …, M. Møller. 2000. Fractal correlation properties of R-R interval dynamics and mortality in patients with depressed left ventricular function after an acute myocardial infarction. *Circulation.* 101:47–53.

10. Woo, M. A., W. G. Stevenson, …, R. M. Harper. 1992. Patterns of beat-to-beat heart rate variability in advanced heart failure. *Am. Heart J.* 123:704–710.

11. Cook, J. R., J. T. Bigger, Jr., …, L. M. Rolnitzky. 1991. Effect of atenolol and diltiazem on heart period variability in normal persons. *J. Am. Coll. Cardiol.* 17:480–484.

12. Mortara, A., M. T. La Rovere, …, F. Cobelli. 2000. Nonselective β-adrenergic blocking agent, carvedilol, improves arterial baroflex gain and heart rate variability in patients with stable chronic heart failure. *J. Am. Coll. Cardiol.* 36:1612–1618.

13. Niemelä, M. J., K. E. Airaksinen, and H. V. Huikuri. 1994. Effect of β-blockade on heart rate variability in patients with coronary artery disease. *J. Am. Coll. Cardiol.* 23:1370–1377.

14. Böhm, M., J. S. Borer, …, K. Swedberg. 2015. Twenty-four-hour heart rate lowering with ivabradine in chronic heart failure: insights from the SHIFT Holter substudy. *Eur. J. Heart Fail.* 17:518–526.

15. Kurtoglu, E., S. Balta, …, G. Gozubuyuk. 2014. Ivabradine improves heart rate variability in patients with nonischemic dilated cardiomyopathy. *Arq. Bras. Cardiol.* 103:308–314.

16. Huikuri, H. V., J. O. Valkama, …, R. J. Myerburg. 1993. Frequency domain measures of heart rate variability before the onset of nonsustained and sustained ventricular tachycardia in patients with coronary artery disease. *Circulation.* 87:1220–1228.

17. Pruvot, E., G. Thonet, …, M. Fromer. 2000. Heart rate dynamics at the onset of ventricular tachyarrhythmias as retrieved from implantable cardioverter-defibrillators in patients with coronary artery disease. *Circulation.* 101:2398–2404.

18. Shusterman, V., B. Aysin, …, K. P. Anderson; ESVEM Investigators. Electrophysiologic Study Versus Electrocardiographic Monitoring Trial. 1998. Autonomic nervous system activity and the spontaneous initiation of ventricular tachycardia. *J. Am. Coll. Cardiol.* 32:1891–1899.

19. Burri, H., P. Chevalier, …, P. Touboul. 2006. Wavelet transform for analysis of heart rate variability preceding ventricular arrhythmias in patients with ischemic heart disease. *Int. J. Cardiol.* 109:101–107.

20. Huikuri, H. V., T. Seppänen, …, R. J. Myerburg. 1996. Abnormalities in beat-to-beat dynamics of heart rate before the spontaneous onset of life-threatening ventricular tachyarrhythmias in patients with prior myocardial infarction. *Circulation.* 93:1836–1844.

21. Vybiral, T., D. H. Glaeser, …, C. M. Pratt. 1993. Conventional heart rate variability analysis of ambulatory electrocardiographic recordings fails to predict imminent ventricular fibrillation. *J. Am. Coll. Cardiol.* 22:557–565.

22. Fox, K., J. S. Borer, …, M. Tendera; Heart Rate Working Group. 2007. Resting heart rate in cardiovascular disease. *J. Am. Coll. Cardiol.* 50:823–830.

23. Jouven, X., J. P. Empana, …, P. Ducimetière. 2005. Heart-rate profile during exercise as a predictor of sudden death. *N. Engl. J. Med.* 352:1951–1958.

24. Abildstrom, S. Z., B. T. Jensen, …, J. K. Kanters; BEAT Study Group. 2003. Heart rate versus heart rate variability in risk prediction after myocardial infarction. *J. Cardiovasc. Electrophysiol.* 14:168–173.

25. Monfredi, O., A. E. Lyashkov, …, M. R. Boyett. 2014. Biophysical characterization of the underappreciated and important relationship between heart rate variability and heart rate. *Hypertension.* 64:1334–1343.

26. Tsuji, H., F. J. Venditti, Jr., …, D. Levy. 1996. Determinants of heart rate variability. *J. Am. Coll. Cardiol.* 28:1539–1546.

27. Anderson, K. P., V. Shusterman, …, V. Gottipaty; Electrophysiologic Study Versus Electrocardiographic Monitoring. 1999. Distinctive RR dynamics preceding two modes of onset of spontaneous sustained ventricular tachycardia. *J. Cardiovasc. Electrophysiol.* 10:897–904.

28. Wollmann, C. G., R. Gradaus, …, G. Breithardt. 2015. Variations of heart rate variability parameters prior to the onset of ventricular tachyarrhythmia and sinus tachycardia in ICD patients. Results from the heart rate variability analysis with automated ICDs (HAWAI) registry. *Physiol. Meas.* 36:1047–1061.

29. Cutler, M. J., and D. S. Rosenbaum. 2009. Explaining the clinical manifestations of T wave alternans in patients at risk for sudden cardiac death. *Heart Rhythm.* 6 (3, Suppl):S22–S28.

30. Gelzer, A. R. M., M. L. Koller, …, R. F. Gilmour, Jr. 2008. Dynamic mechanism for initiation of ventricular fibrillation in vivo. *Circulation.* 118:1123–1129.

31. Narayan, S. M. 2006. T-wave alternans and the susceptibility to ventricular arrhythmias. *J. Am. Coll. Cardiol.* 47:269–281.

32. Pastore, J. M., S. D. Girouard, …, D. S. Rosenbaum. 1999. Mechanism linking T-wave alternans to the genesis of cardiac fibrillation. *Circulation.* 99:1385–1394.

33. Pastore, J. M., and D. S. Rosenbaum. 2000. Role of structural barriers in the mechanism of alternans-induced reentry. *Circ. Res.* 87:1157–1163.

34. Qu, Z., A. Garfinkel, …, J. N. Weiss. 2000. Mechanisms of discordant alternans and induction of reentry in simulated cardiac tissue. *Circulation.* 102:1664–1670.

35. Watanabe, M. A., F. H. Fenton, …, A. Karma. 2001. Mechanisms for discordant alternans. *J. Cardiovasc. Electrophysiol.* 12:196–206.

36. Nolasco, J. B., and R. W. Dahlen. 1968. A graphic method for the study of alternation in cardiac action potentials. *J. Appl. Physiol.* 25:191–196.

37. Pruvot, E. J., R. P. Katra, …, K. R. Laurita. 2004. Role of calcium cycling versus restitution in the mechanism of repolarization alternans. *Circ. Res.* 94:1083–1090.

38. Qu, Z., M. Nivala, and J. N. Weiss. 2013. Calcium alternans in cardiac myocytes: order from disorder. *J. Mol. Cell. Cardiol.* 58:100–109.

39. Groenendaal, W., F. A. Ortega, …, D. J. Christini. 2014. Voltage and calcium dynamics both underlie cellular alternans in cardiac myocytes. *Biophys. J.* 106:2222–2232.

40. Echebarria, B., and A. Karma. 2002. Instability and spatiotemporal dynamics of alternans in paced cardiac tissue. *Phys. Rev. Lett.* 88:208101.

41. Skardal, P. S., A. Karma, and J. G. Restrepo. 2012. Unidirectional pinning and hysteresis of spatially discordant alternans in cardiac tissue. *Phys. Rev. Lett.* 108:108103.

42. Laurita, K. R., S. D. Girouard, and D. S. Rosenbaum. 1996. Modulation of ventricular repolarization by a premature stimulus. Role of epicardial dispersion of repolarization kinetics demonstrated by optical mapping of the intact guinea pig heart. *Circ. Res.* 79:493–503.

43. Krogh-Madsen, T., and D. J. Christini. 2007. Action potential duration dispersion and alternans in simulated heterogeneous cardiac tissue with a structural barrier. *Biophys. J.* 92:1138–1149.

44. de Diego, C., R. K. Pai, …, M. Valderrábano. 2008. Spatially discordant alternans in cardiomyocyte monolayers. *Am. J. Physiol. Heart Circ. Physiol.* 294:H1417–H1425.

45. Gizzi, A., E. M. Cherry, …, F. H. Fenton. 2013. Effects of pacing site and stimulation history on alternans dynamics and the development of complex spatiotemporal patterns in cardiac tissue. *Front. Physiol.* 4:71.

46. Hayashi, H., Y. Shiferaw, …, Z. Qu. 2007. Dynamic origin of spatially discordant alternans in cardiac tissue. *Biophys. J.* 92:448–460.

47. Mironov, S., J. Jalife, and E. G. Tolkacheva. 2008. Role of conduction velocity restitution and short-term memory in the development of action potential duration alternans in isolated rabbit hearts. *Circulation.* 118:17–25.

48. Ziv, O., E. Morales, …, B. R. Choi. 2009. Origin of complex behaviour of spatially discordant alternans in a transgenic rabbit model of type 2 long QT syndrome. *J. Physiol.* 587:4661–4680.

49. Dekker, J. M., R. S. Crow, …, E. G. Schouten. 2000. Low heart rate variability in a 2-minute rhythm strip predicts risk of coronary heart disease and mortality from several causes: the ARIC Study. Atherosclerosis risk in communities. *Circulation.* 102:1239–1244.

50. Dekker, J. M., E. G. Schouten, …, D. Kromhout. 1997. Heart rate variability from short electrocardiographic recordings predicts mortality from all causes in middle-aged and elderly men. The Zutphen study. *Am. J. Epidemiol.* 145:899–908.

51. Nolan, J., P. D. Batin, …, K. A. A. Fox. 1998. Prospective study of heart rate variability and mortality in chronic heart failure: results of the United Kingdom heart failure evaluation and assessment of risk trial (UK-heart). *Circulation.* 98:1510–1516.

52. Tsuji, H., M. G. Larson, …, D. Levy. 1996. Impact of reduced heart rate variability on risk for cardiac events. The Framingham Heart Study. *Circulation.* 94:2850–2855.

53. Braga, A. N. G., M. da Silva Lemos, …, R. A. S. dos Santos. 2002. Effects of angiotensins on day-night fluctuations and stress-induced changes in blood pressure. *Am. J. Physiol. Regul. Integr. Comp. Physiol.* 282:R1663–R1671.

54. Aoki, K., D. P. Stephens, and J. M. Johnson. 2001. Diurnal variation in cutaneous vasodilator and vasoconstrictor systems during heat stress. *Am. J. Physiol. Regul. Integr. Comp. Physiol.* 281:R591–R595.

55. Pagani, M., F. Lombardi, …, A. Malliani. 1986. Power spectral analysis of heart rate and arterial pressure variabilities as a marker of sympatho-vagal interaction in man and conscious dog. *Circ. Res.* 59:178–193.

56. Hayano, J., Y. Sakakibara, …, K. Takata. 1991. Accuracy of assessment of cardiac vagal tone by heart rate variability in normal subjects. *Am. J. Cardiol.* 67:199–204.

57. Akselrod, S., D. Gordon, …, R. J. Cohen. 1981. Power spectrum analysis of heart rate fluctuation: a quantitative probe of beat-to-beat cardiovascular control. *Science.* 213:220–222.

58. McIntyre, S. D., V. Kakade, …, E. G. Tolkacheva. 2014. Heart rate variability and alternans formation in the heart: The role of feedback in cardiac dynamics. *J. Theor. Biol.* 350:90–97.

59. Prudat, Y., R. V. Madhvani, …, J. P. Kucera. 2016. Stochastic pacing reveals the propensity to cardiac action potential alternans and uncovers its underlying dynamics. *J. Physiol.* 594:2537–2553.

60. Dvir, H., and S. Zlochiver. 2013. Stochastic cardiac pacing increases ventricular electrical stability—a computational study. *Biophys. J.* 105:533–542.

61. Shiferaw, Y., D. Sato, and A. Karma. 2005. Coupled dynamics of voltage and calcium in paced cardiac cells. *Phys. Rev. E Stat. Nonlin. Soft Matter Phys.* 71:021903.

62. Rush, S., and H. Larsen. 1978. A practical algorithm for solving dynamic membrane equations. *IEEE Trans. Biomed. Eng.* 25:389–392.

63. Moore, J. W., and F. Ramon. 1974. On numerical integration of the Hodgkin and Huxley equations for a membrane action potential. *J. Theor. Biol.* 45:249–273.

64. Fox, J. J., J. L. McHarg, and R. F. Gilmour, Jr. 2002. Ionic mechanism of electrical alternans. *Am. J. Physiol. Heart Circ. Physiol.* 282:H516–H530.

65. Clayton, R. H., O. Bernus, …, H. Zhang. 2011. Models of cardiac tissue electrophysiology: progress, challenges and open questions. *Prog. Biophys. Mol. Biol.* 104:22–48.

66. Näbauer, M., D. J. Beuckelmann, …, G. Steinbeck. 1996. Regional differences in current density and rate-dependent properties of the transient outward current in subepicardial and subendocardial myocytes of human left ventricle. *Circulation.* 93:168–177.

67. Cherry, E. M., and F. H. Fenton. 2011. Effects of boundaries and geometry on the spatial distribution of action potential duration in cardiac tissue. *J. Theor. Biol.* 285:164–176.

68. Myles, R. C., O. Bernus, …, G. L. Smith. 2010. Effect of activation sequence on transmural patterns of repolarization and action potential duration in rabbit ventricular myocardium. *Am. J. Physiol. Heart Circ. Physiol.* 299:H1812–H1822.

69. Osaka, T., I. Kodama, …, K. Yamada. 1987. Effects of activation sequence and anisotropic cellular geometry on the repolarization phase of action potential of dog ventricular muscles. *Circulation.* 76:226–236.

70. Restrepo, J. G., and A. Karma. 2009. Spatiotemporal intracellular calcium dynamics during cardiac alternans. *Chaos.* 19:037115.

71. Zhao, X. 2008. Indeterminacy of spatiotemporal cardiac alternans. *Phys. Rev. E Stat. Nonlin. Soft Matter Phys.* 78:011902.

72. Bers, D. M. 2002. Cardiac excitation-contraction coupling. *Nature.* 415:198–205.

73. Sato, D., Y. Shiferaw, …, A. Karma. 2006. Spatially discordant alternans in cardiac tissue: role of calcium cycling. *Circ. Res.* 99:520–527.

74. Meyer, C. D. 2000. Matrix Analysis and Applied Linear Algebra.Volume 2. Siam, Philadelphia, PA.

75. Choi, B. R., and G. Salama. 2000. Simultaneous maps of optical action potentials and calcium transients in guinea-pig hearts: mechanisms underlying concordant alternans. *J. Physiol.* 529:171–188.

76. Goldhaber, J. I., L. H. Xie, …, J. N. Weiss. 2005. Action potential duration restitution and alternans in rabbit ventricular myocytes: the key role of intracellular calcium cycling. *Circ. Res.* 96:459–466.

77. Weiss, J. N., A. Karma, …, Z. Qu. 2006. From pulsus to pulseless: the saga of cardiac alternans. *Circ. Res.* 98:1244–1253.

78. Gardiner, C. W. 2004. Handbook of Stochastic Methods: for Physics, Chemistry and the Natural Sciences.. Springer, Berlin, Germany.

79. Echebarria, B., and A. Karma. 2007. Amplitude equation approach to spatiotemporal dynamics of cardiac alternans. *Phys. Rev. E Stat. Nonlin. Soft Matter Phys.* 76:051911.

80. Cherry, E. M., and S. J. Evans. 2008. Properties of two human atrial cell models in tissue: restitution, memory, propagation, and reentry. *J. Theor. Biol.* 254:674–690.

81. Tolkacheva, E. G., D. G. Schaeffer, …, W. Krassowska. 2003. Condition for alternans and stability of the 1:1 response pattern in a "memory" model of paced cardiac dynamics. *Phys. Rev. E Stat. Nonlin. Soft Matter Phys.* 67:031904.

82. Christini, D. J., M. L. Riccio, …, R. F. Gilmour, Jr. 2006. Control of electrical alternans in canine cardiac Purkinje fibers. *Phys. Rev. Lett.* 96:104101.

83. Garzón, A., R. O. Grigoriev, and F. H. Fenton. 2014. Continuous-time control of alternans in long Purkinje fibers. *Chaos.* 24:033124.

84. Wilson, D., and J. Moehlis. 2017. Spatiotemporal control to eliminate cardiac alternans using isostable reduction. *Physica D.* 342:32–44.

85. Echebarria, B., and A. Karma. 2002. Spatiotemporal control of cardiac alternans. *Chaos.* 12:923–930.

86. Blatter, L. A., J. Kockskämper, …, S. L. Lipsius. 2003. Local calcium gradients during excitation-contraction coupling and alternans in atrial myocytes. *J. Physiol.* 546:19–31.

87. Skardal, P. S., A. Karma, and J. G. Restrepo. 2014. Spatiotemporal dynamics of calcium-driven cardiac alternans. *Phys. Rev. E Stat. Nonlin. Soft Matter Phys.* 89:052707.

88. Cherry, E. M., and F. H. Fenton. 2004. Suppression of alternans and conduction blocks despite steep APD restitution: electrotonic, memory, and conduction velocity restitution effects. *Am. J. Physiol. Heart Circ. Physiol.* 286:H2332–H2341.

89. Hall, G. M., S. Bahar, and D. J. Gauthier. 1999. Prevalence of rate-dependent behaviors in cardiac muscle. *Phys. Rev. Lett.* 82:2995–2998.

90. Hespanha, J. P. 2009. Linear Systems Theory.. Princeton University Press, Princeton, NJ.